

## Electronic Supplementary Information

### Structural Evolution of Water Oxidation Catalyst by Incorporation of High-Valent Vanadium from Electrolyte Solution

Baghendra Singh,<sup>a</sup> Yu-Cheng Huang,<sup>b</sup> Adyasa Priyadarsini,<sup>c</sup> Pandian Mannu,<sup>b</sup> Sanchaita Dey,<sup>d</sup> Goutam Kumar Lahiri,<sup>d\*</sup> Bhabani S. Mallik,<sup>c\*</sup> Chung-Li Dong,<sup>b\*</sup> and Arindam Indra<sup>a\*</sup>

<sup>a</sup>Department of Chemistry, Indian Institute of Technology (BHU), Varanasi, Uttar Pradesh-221005, India  
E-mail: [arindam.chy@iitbhu.ac.in](mailto:arindam.chy@iitbhu.ac.in)

<sup>b</sup>Department of Physics, Tamkang University, New Taipei City, Taiwan  
E-mail: [cldong@mail.tku.edu.tw](mailto:cldong@mail.tku.edu.tw)

<sup>c</sup>Department of Chemistry, Indian Institute of Technology Hyderabad, Sangareddy, Telangana-502285, India  
E-mail: [bhabani@chy.iith.ac.in](mailto:bhabani@chy.iith.ac.in)

<sup>d</sup>Department of Chemistry, Indian Institute of Technology Bombay, Powai-400076, Mumbai, Maharashtra, India  
E-mail: [lahiri@chem.iitb.ac.in](mailto:lahiri@chem.iitb.ac.in)

## Chemicals

The chemicals were used as received from the manufacturers without further purification. The  $\text{NiCl}_2 \cdot 6\text{H}_2\text{O}$ ,  $\text{NH}_2\text{CONH}_2$  were procured from MERCK Life Sciences Pvt. Ltd. India, and  $\text{NH}_4\text{F}$  was purchased from SRL Pvt. Ltd. India. The  $\text{K}_2[\text{Ni}(\text{CN})_4]$  was bought from Sigma-Aldrich. Nickel foam was purchased from Axys Technology, Kolkata, India.  $\text{VOSO}_4$  was bought from Sigma-Aldrich. The washing, synthesis, and electrochemical measurements were performed using double distilled water.

## Instruments

The powder X-ray diffraction (PXRD) measurements were conducted on a Rigaku D/MAX RINT-2000 X-Ray diffractometer to evaluate the crystal structure and phases of the synthesized catalysts. The  $\text{Cu-K}_\alpha$  ( $\lambda = 1.5418 \text{ \AA}$ ) radiation was used for the PXRD measurements. The PXRD patterns were recorded in the range of  $5^\circ < 2\theta < 80^\circ$ . A Thermo Scientific Nicolet iS5 FTIR spectrometer was utilized to record IR spectra of the synthesized materials under attenuated total reflection (ATR) mode.

The chemical state, bonding situation, and surface structure of the synthesized catalysts were examined by X-ray photoelectron spectroscopy (XPS) using VG/VG ESCA LAB 220i X-ray photoelectron spectrometer. The XPS data were analyzed using Origin 8.5 software.

The scanning electron microscopy (SEM) was performed to investigate the morphology and surface characteristics using field emission scanning electron microscope EVO-Scanning Electron Microscope MA15/18. Energy dispersive X-ray (EDX) analysis was carried out on Team Pegasus Integrated EDS-EBSD. Tecnai G2 F30 TWIN transmission electron microscope was utilized for the transmission electron microscopic (TEM) studies. A small piece of the catalyst film was sonicated in 2 mL ethanol for 10 min and the well-dispersed particles were drop cast on a Cu grid for the TEM measurements. The atomic force microscopic (AFM) studies were carried out using NTEGRA Prima scanning probe microscope.

Synchrotron X-ray absorption near-edge structure (XANES) and the Extended X-ray absorption fine structure (EXAFS) were measured at beamline BL17C, which is equipped with a Si(111) double-crystal monochromator, at Taiwan Light Source (TLS) of the National Synchrotron Radiation Research Center (NSRRC), Taiwan. The storage ring of TLS operates at 1.5 GeV with a current of about 360 mA. The spectra were collected in transmission mode. Raw data were analyzed following standard procedures, including pre-edge and post-edge background subtractions, normalization for the edge jump, and Fourier transformation. The energy resolutions of hard XAS (Ni K-edge) and soft XAS (Ni L-edge) were set to 0.3 and 0.1 eV, respectively.

## Experimental

### Activation of nickel foam (NF)<sup>1</sup>

The nickel foam was cut into the pieces of  $1 \times 2 \text{ cm}^2$  and cleaned with acetone and water. Further, the pieces of nickel foams were treated with 3.0 M HCl for 15 min under ultra-sonication conditions to remove the surface impurities. The pre-treated NF was utilized for the synthesis of the catalysts.

### Synthesis of nickel hydroxide carbonate on nickel foam [NiHC@NF]<sup>2</sup>

A mixture was prepared by dissolving 2 mmol  $\text{NiCl}_2 \cdot 6\text{H}_2\text{O}$ , 4 mmol  $\text{NH}_4\text{F}$ , and 10 mmol  $\text{NH}_2\text{CONH}_2$  in water (12 mL). The solution was placed into a 40 mL Teflon coated autoclave and pieces of nickel foam were dipped

vertically inside the mixture. Further, the autoclave was sealed and heated at 120 °C for 5 h. After normal cooling to room temperature, the films of NiHC@NF were washed with water and ethanol and then dried in an air oven at 50 °C for 12 h.

### Synthesis of Ni-CP@NF

A homogeneous solution of 0.4 mmol of  $K_2[Ni(CN)_4]$  was prepared in 5 mL of water in a glass vial. A piece of NiHC@NF were placed inside the solution and kept at room temperature for 1 h. Further, the glass vial was capped and heated at 60 °C in an air oven for 6 h. As synthesized Ni-CP@NF films were washed with water several times and dried at 50 °C overnight.

### Electrochemical reconstruction of Ni-CP@NF precatalyst into V-Ni(OH)<sub>2</sub>/Ni(O)OH (VNi-AC-1) and Ni(OH)<sub>2</sub>/Ni(O)OH (Ni-AC-1)

The synthesized precatalyst Ni-CP@NF was treated under cyclic voltammetric (CV) conditions with the precatalyst@NF as working electrode, Ag/AgCl as reference electrode, and Pt wire as the counter electrode. The CV was performed at the scan rate of 20 mV s<sup>-1</sup> for 200 cycles in 1.0 M aqueous KOH solution. As a result, the Ni(OH)<sub>2</sub>/Ni(O)OH (denoted as Ni-AC-1) was formed by the electrochemical reconstruction of Ni-CP.

For the synthesis of V-Ni(OH)<sub>2</sub>/Ni(O)OH (denoted as VNi-AC-1), 20 mg VOSO<sub>4</sub> was added into the 12 mL of 1.0 M aqueous KOH solution and the cyclic voltammetry was carried out for 200 cycles at the same scan rate. Interestingly, V was incorporated into the Ni(OH)<sub>2</sub>/Ni(O)OH during the electrochemical reconstruction within 200 CV cycles to form V-Ni(OH)<sub>2</sub>/Ni(O)OH active catalyst.

Similarly, different amount of VOSO<sub>4</sub> (10 mg and 30 mg) was added into the electrolyte to synthesize the active V-Ni(OH)<sub>2</sub>/Ni(O)OH catalysts (denoted as VNi-AC-2 and VNi-AC-3), respectively. The CV studies showed the stabilization of the CV profiles within 200 CV cycles while the IR spectra showed that the –CN peak in CP was completely disappeared within 200 CV cycles indicating the complete transformation.

### Electrochemical reconstruction of Ni-CP@NF precatalyst into Ni(OH)<sub>2</sub>/Ni(O)OH (Ni-AC-2)

The synthesized precatalyst Ni-CP@NF was treated under CV conditions in 1.0 M aqueous KOH solution having 20 mg of NiCl<sub>2</sub>·6H<sub>2</sub>O. The cyclic voltammetry was carried out at the scan rate of 20 mV s<sup>-1</sup> for 200 cycles to form Ni(OH)<sub>2</sub>/Ni(O)OH (denoted as Ni-AC-2).

**Table S1.** The different active catalysts synthesized by the electrochemical transformation of precatalysts and their reaction conditions.

Sr. No.	Precatalyst	Electrochemical condition	Metal salt amount	Active catalyst	Denoted name
1	Ni-CP	200 CV-cycles, 1-2 V vs RHE	10 mM VOSO <sub>4</sub>	V-Ni(OH) <sub>2</sub> /Ni(O)OH	VNi-AC-1
2	Ni-CP	200 CV-cycles, 1-2 V vs RHE	5 mM VOSO <sub>4</sub>	V-Ni(OH) <sub>2</sub> /Ni(O)OH	VNi-AC-2
3	Ni-CP	200 CV-cycles, 1-2 V vs RHE	15 mM VOSO <sub>4</sub>	V-Ni(OH) <sub>2</sub> /Ni(O)OH	VNi-AC-3

		RHE		Ni(OH) <sub>2</sub> /Ni(O)OH	
4	Ni-CP	200 CV-cycles, 1-2 V vs RHE	-	Ni(OH) <sub>2</sub> /Ni(O)OH	Ni-AC-1
5	Ni-CP	200 CV-cycles, 1-2 V vs RHE	10 mM NiCl <sub>2</sub> .6H <sub>2</sub> O	Ni(OH) <sub>2</sub> /Ni(O)OH	Ni-AC-2

**Table S2.** The amount of V incorporation in the active catalyst determined by EDX spectroscopy.

Sr. No.	Active catalysts	Amount of Ni (atomic %)	Amount of V (atomic %)	Amount of O (atomic %)
1	VNi-AC-1	55.12%	5.4%	39.48%

### Electrochemical measurements

The electrochemical measurements were carried out in a single-compartment three-electrode electrochemical cell in a 1.0 M aqueous KOH solution. The precatalyst films on nickel foam were used as the working electrode and Pt wire was used as the counter electrode while Ag/AgCl electrode was used as the reference electrode in 1.0 M aqueous KOH solution (pH 13.8). Cyclic voltammetry (CV) and linear sweep voltammetry (LSV) were recorded and represented with 60% iR compensation. All the potentials were represented against reversible hydrogen electrode (RHE) by using the formula:

$$E(\text{RHE}) = E(\text{Ag/AgCl}) + 0.197 + 0.059\text{pH}$$

Electrochemical impedance spectroscopic (EIS) measurements were recorded in the frequency range from 0.001 to 100,000 Hz and amplitude of 10 mV. The charge transfer resistance ( $R_{ct}$ ) was calculated from the diameter of the semicircle in the Nyquist plots.

The chronoamperometric measurements (CA) were carried out in 1.0 M aqueous KOH at selected constant potentials and represented without iR compensation. Tafel plots were determined by potentiostatic measurements at the potentials where current density was reached up to 10 mA cm<sup>-2</sup>. The Tafel slope was calculated using the Tafel equation:

$$\eta = b \log j + a$$

where  $\eta$  denotes the overpotential (V),  $j$  is the current density (mA cm<sup>-2</sup>), and  $b$  is the Tafel slope (mV dec<sup>-1</sup>). The electrochemically active surface areas (ECSAs) were directly related to the double-layer capacitance ( $C_{dl}$ ). For  $C_{dl}$  measurements, CV was carried out at a potential range of 0.90 to 1.00 V vs RHE in non-faradaic region.

### Computational calculations

The density functional theory (DFT) calculations were performed to find a better insight into the OER supported by V-doped Ni(OH)<sub>2</sub>. Experimentally we find that the VNi-AC-1 with a Ni:V atomic ratio of 93.4:6.6 performs best as the OER catalyst. Therefore, we selected the V-incorporated model system for

computational investigations. Previous theoretical studies revealed that the undercoordinated sites only acted as oxo-intermediate adsorption sites.<sup>3</sup> Thus, we carved the  $(-121) \approx (1\bar{2}\bar{1}1)$  facet and doped a vanadium atom replacing one nickel atom. The unit cell parameters of the carved surface are  $a=11.20 \text{ \AA}$ ,  $b=10.96 \text{ \AA}$ ,  $c=6.33 \text{ \AA}$ ,  $\alpha=90^\circ$ ,  $\beta=106.30^\circ$ ,  $\gamma=60.96^\circ$ . Hence carved  $(1\bar{2}\bar{1}1)$  unit cell was repeated  $2 \times 2 \times 2$  to obtain the supercell with a total of 16 nickel atoms. The experimental doping consistency was achieved by replacing one nickel atom with vanadium. A vacuum space of  $10 \text{ \AA}$  was added to avoid self-interaction among periodic images of the slab and the surface adsorbed species. Spin-polarized DFT calculations were performed using Vienna Ab initio Simulation Package (VASP).<sup>4,5</sup> Perdew–Burke–Ernzerhof (PBE)<sup>6</sup> exchange-correlation function along with Grimme’s 3<sup>rd</sup> order dispersion corrections<sup>7,8</sup> were used to calculate the energies. Projector augmented wave (PAW)<sup>7,8</sup> with a 600 eV energy cutoff was used throughout the study. A Monkhorst pack scheme<sup>9</sup> of  $3 \times 3 \times 1$  was used. Energy optimizations were performed with Gaussian smearing till the energy and force tolerance reached less than  $1 \times 10^{-6} \text{ \AA}$  and  $1 \times 10^{-2} \text{ eV \AA}^{-1}$ . The surface extraction was done so that the outermost surface metal atoms had 4 bridging oxygens, shared with adjacent metal sites, and one dangling OH. The nomenclature of the different intermediates is done considering the dangling oxygen-based species; for example, if the Ni atom is attached with OH and O, it is denoted as Ni-OH-O. We have followed a similar protocol throughout the paper. The experiments were performed in 1.0 M KOH solution. Thus, we performed a single-point calculation in the implicit solvation environment using VASPsol.<sup>10,11</sup> The dielectric constant of the 1 M KOH was set to (EK\_B) 69.8.<sup>12</sup> The elementary reaction steps in different pathways were equilibrated using  $\text{OH}^-$ , hence we followed the computational hydrogen electrode (CHE) model<sup>13,14</sup> implemented by Norskov and used the chemical potential of water (liquid), oxygen (gas),  $\text{OH}^-$  to equate the difference in the free energy in the consecutive steps. The standard CHE model follows the hydrogen activity as a descriptor hence the standard hydrogen electrode (SHE) as the reference electrode. However, our equilibration method uses hydroxide ( $\text{OH}^-$ ). Following this, we need to use  $\text{OH}^-$  chemical potential as a descriptor, given as,

$$\mu_{\text{OH}^-} - \mu_{e^-} = \mu_{\text{H}_2\text{O}(l)} - \mu_{\text{H}^+} + \mu_{e^-} = \mu_{\text{H}_2\text{O}(l)} - \left(\frac{1}{2} \mu_{\text{H}_2(\text{g})} - eU_{\text{RHE}}\right) \quad (1)$$

Following the recently devised Liang’s approach for the CHE model,<sup>15</sup> we do not require the slab +  $\text{O}_2$  energy and can simply add the molecular gaseous oxygen energy for the steps involving oxygen desorption. However, due to difficulties in the description of  $\text{O}_2$  through DFT, its chemical potential is equated to water as,

$$\mu_{\text{O}_2(\text{g})} = 2G_{\text{H}_2\text{O}(l)} + \Delta G_0 - 2G_{\text{H}_2(\text{g})}, \Delta G_0 = 4.92 \text{ eV} \quad (2)$$

Using equations (1) and (2) we can model the OER pathway following the reactant, products, and byproducts involved. The free energy differences for the step1-4 are given as,

$$\Delta G_1 = G_{\text{Ni-OH-OH}} - G_{\text{Ni-OH}} - G_{\text{OH}^-} = G_{\text{Ni-OH-OH}} - G_{\text{Ni-OH}} - G_{\text{H}_2\text{O}} + \frac{1}{2}G_{\text{H}_2} - eU_{\text{RHE}} \quad (3)$$

$$\Delta G_2 = G_{\text{Ni-OH-O}} - G_{\text{Ni-OH-OH}} + G_{\text{H}_2\text{O}} - G_{\text{OH}^-} = G_{\text{Ni-OH-O}} - G_{\text{Ni-OH-OH}} + \frac{1}{2}G_{\text{H}_2} - eU_{\text{RHE}} \quad (4)$$

$$\Delta G_3 = G_{\text{Ni-OH-OOH}} - G_{\text{Ni-OH-O}} - G_{\text{OH}^-} = G_{\text{Ni-OH-OOH}} - G_{\text{Ni-OH-O}} - G_{\text{H}_2\text{O}} + \frac{1}{2}G_{\text{H}_2} - eU_{\text{RHE}} \quad (5)$$

$$\begin{aligned} \Delta G_4 &= G_{\text{Ni-OH}} - G_{\text{Ni-OH-OOH}} + G_{\text{O}_2} + G_{\text{H}_2\text{O}} - G_{\text{OH}^-} = G_{\text{Ni-OH}} - G_{\text{Ni-OH-OOH}} + G_{\text{O}_2} + \frac{1}{2}G_{\text{H}_2} \\ &= G_{\text{Ni-OH}} - G_{\text{Ni-OH-OOH}} + 2G_{\text{H}_2\text{O}} - 2G_{\text{H}_2} + \frac{1}{2}G_{\text{H}_2} + 4.92 - eU_{\text{RHE}} \end{aligned} \quad (6)$$

The step with maximum energy difference is considered the rate-determining step (RDS) and the overpotential depends on it as,  $\eta = \Delta G_{max}/1.23 \text{ V}$ , considering the reversible hydrogen electrode (RHE). All the free energy calculations provided below are in reference to  $0 \text{ V } U_{RHE}$ .

## Figures

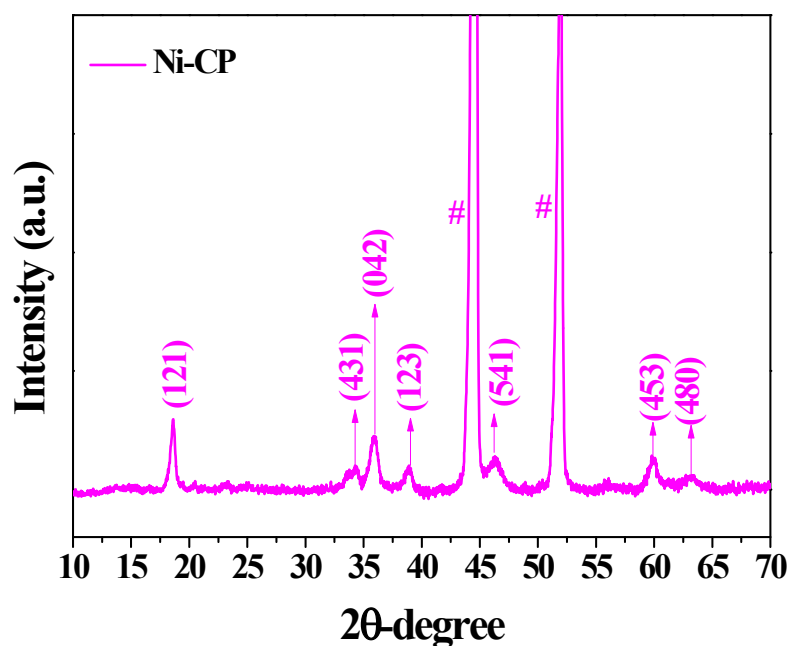


**Figure S1.** The PXRD pattern of Ni-CP. The peaks were well indexed for the Ni-CP. All the diffraction peaks were unambiguously assigned to the Hofmann-type  $\text{Ni}(\text{H}_2\text{O})_2[\text{Ni}(\text{CN})_4] \cdot x\text{H}_2\text{O}$ -CP with a 2D layered structure, which was also consistent with the reported literature. The # marked peaks were originated from the nickel foam.<sup>16-18</sup>

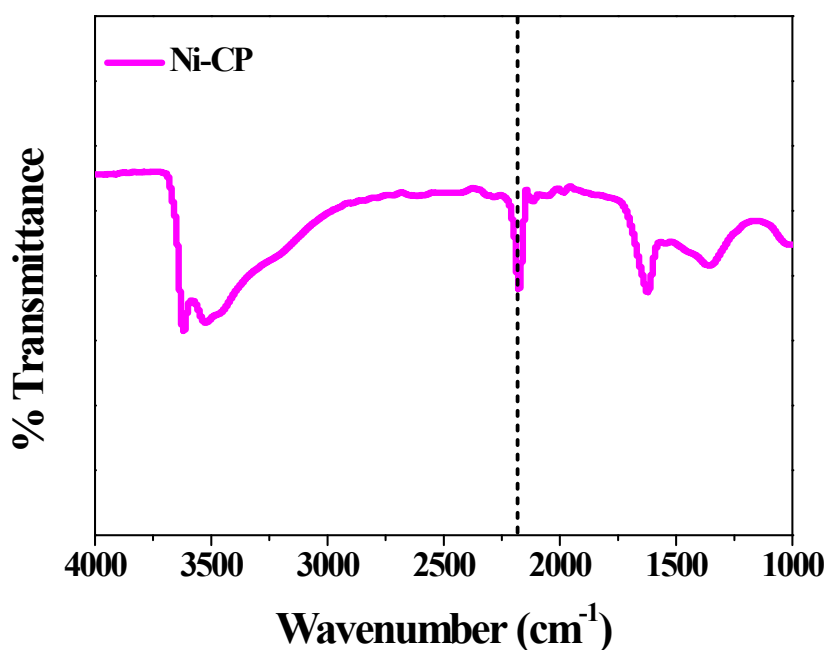


**Figure S2.** IR spectrum of Ni-CP showing the peak for the stretching vibration of  $\text{-CN}$  at  $2175\text{ cm}^{-1}$ .<sup>1,2,19</sup>

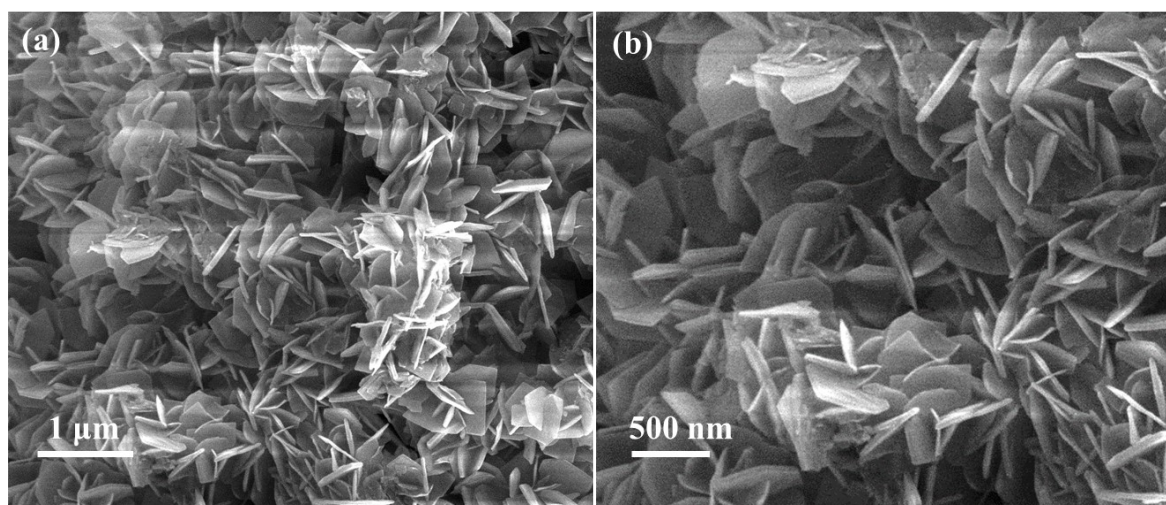


**Figure S3.** (a-b) SEM images of the Ni-CP at different resolutions showing the nanoplate like morphology.

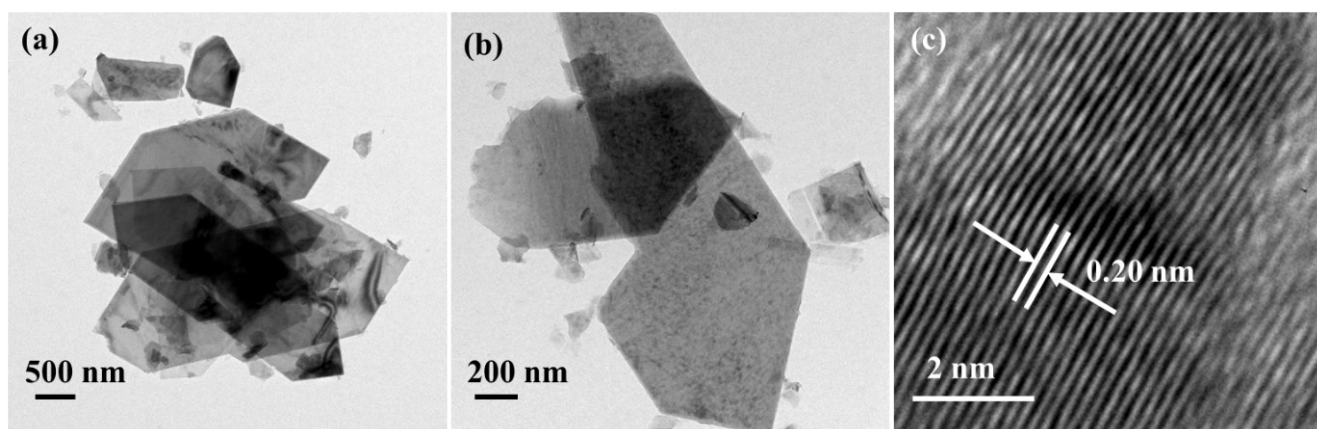


**Figure S4.** (a-b) TEM images of Ni-CP at different resolutions confirming the nanoplate like morphology and (c) HRTEM image showing the d-spacing of 0.20 nm corresponding to the (541) plane of Ni-CP.<sup>16,17</sup>

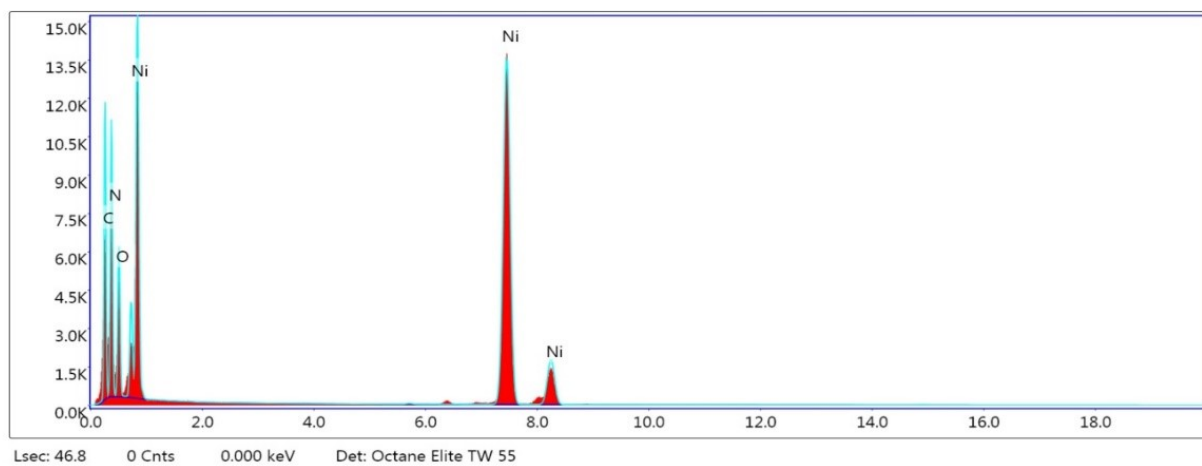


**Figure S5.** EDX spectrum of Ni-CP showing the presence of Ni, C, N and O elements.

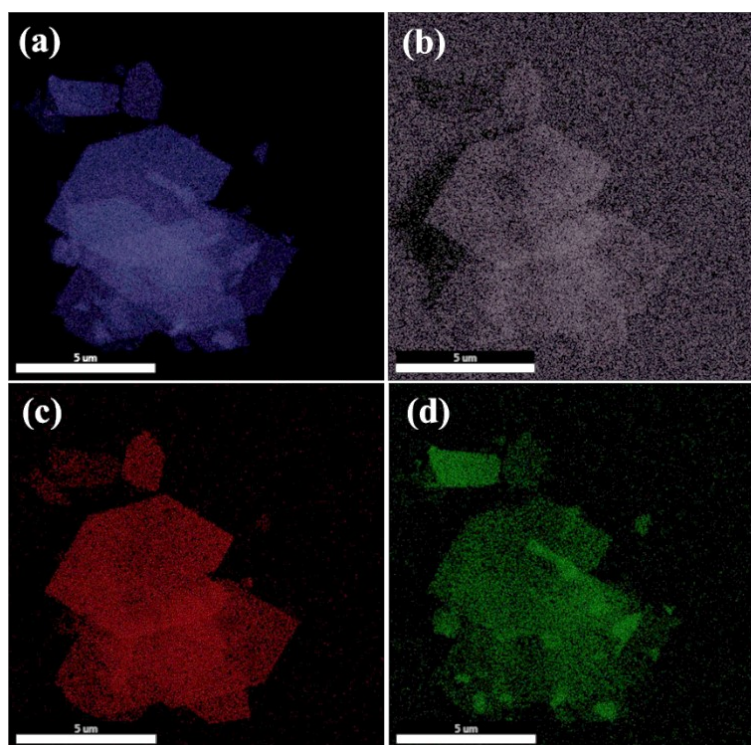


**Figure S6.** Elemental mapping images of (a) Ni; (b) C; (c) N; (d) O showing the homogeneous distribution of elements in Ni-CP.

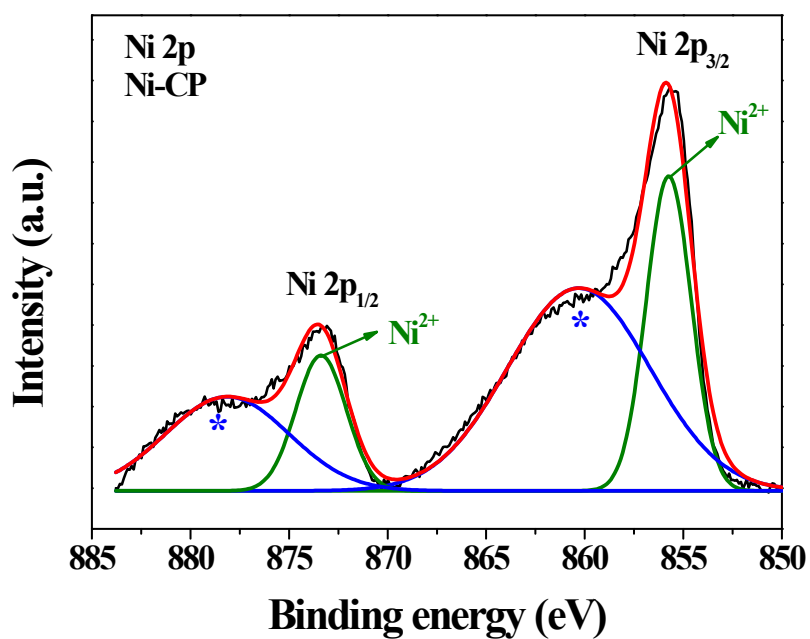


**Figure S7.** Ni 2p XPS of Ni-CP depicting two peaks at 855.52 eV and 873.32 eV for Ni 2p<sub>3/2</sub> and Ni 2p<sub>1/2</sub>, respectively. The peak at 855.74 eV was consigned to the Ni<sup>2+</sup> species while the \* marked peaks were assigned to the satellite peak.<sup>20,21</sup>

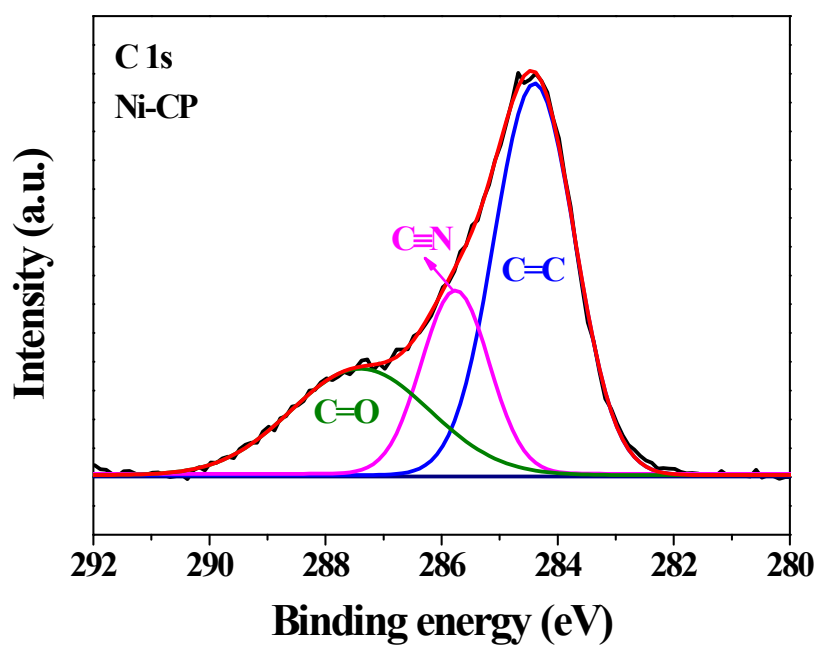


**Figure S8.** C 1s XPS of Ni-CP demonstrating three peaks at 284.38 eV, 285.74 eV, and 287.04 eV related to the C=C, C≡N, and C=O bond, respectively.<sup>2,19</sup>

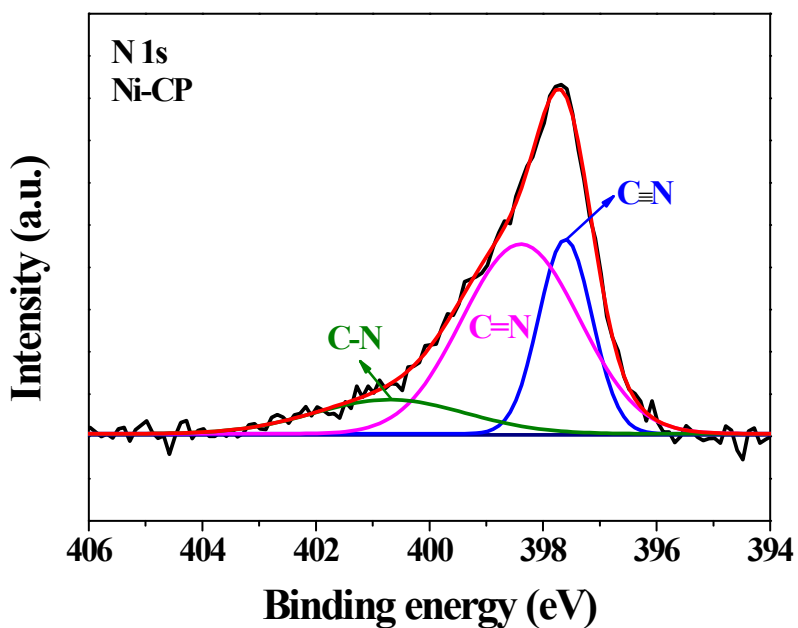


**Figure S9.** N 1s XPS of Ni-CP illustrating the peaks at 397.60 eV, 398.40 eV, and 400.70 eV allocated to the C≡N, C=N, and C-N bond, respectively.<sup>2,19</sup>

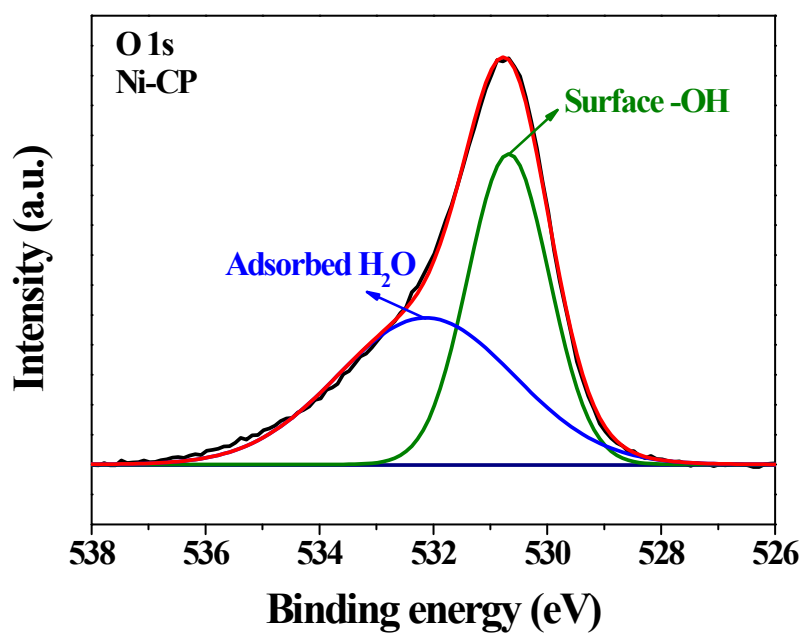


**Figure S10.** O 1s XPS of Ni-CP representing the two peaks at 530.67 eV, and 532.11 eV ascribed to the surface –OH group and adsorbed water molecules, respectively.<sup>2,19</sup>

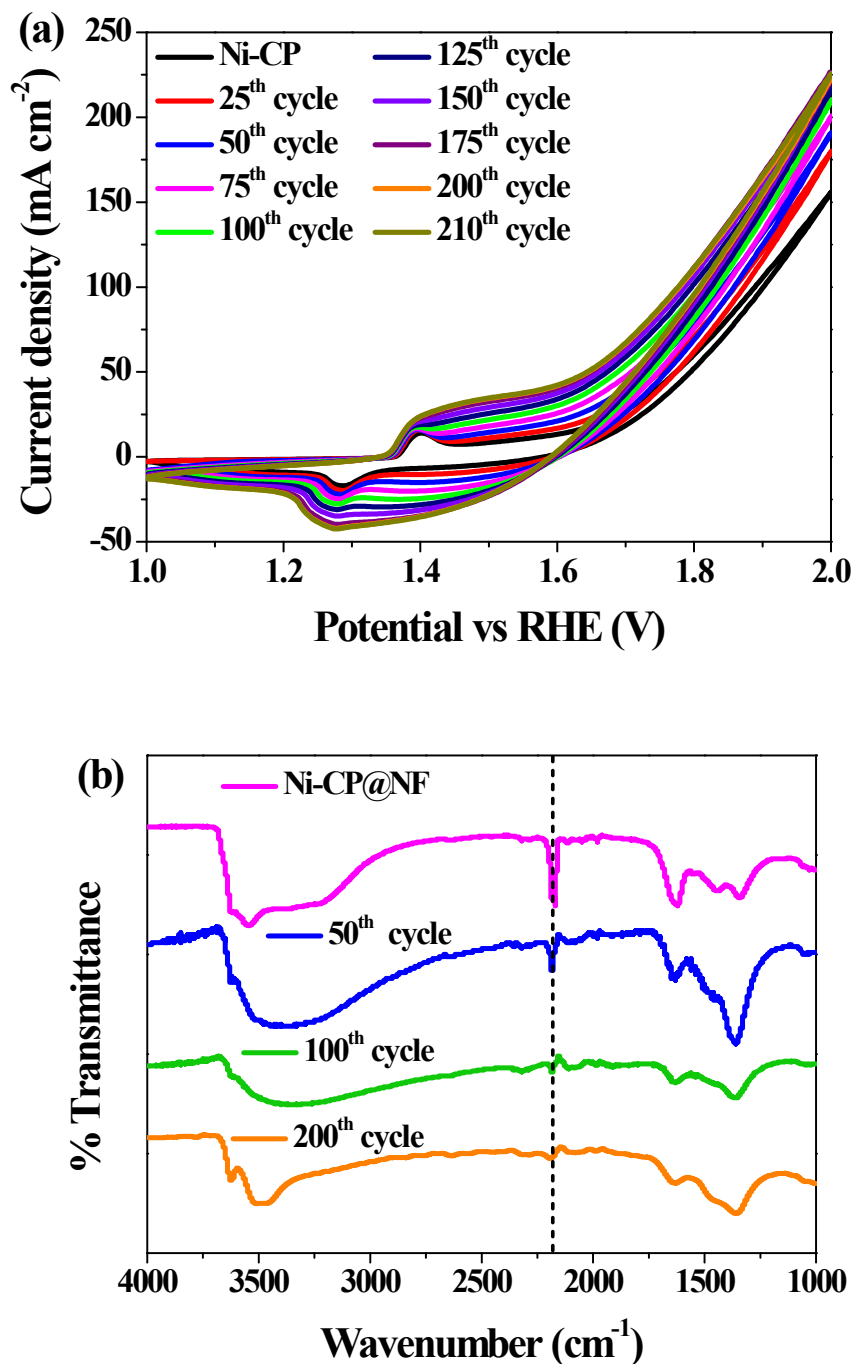


**Figure S11.** (a) CV profiles during the electrochemical activation of Ni-CP into Ni-AC-1, the CV profile revealed the electrochemical activation of Ni-CP into Ni-AC-1 for 200 CV cycles and (b) IR spectra during

electrochemical reconstruction of Ni-CP into Ni-AC-1 at different CV cycles, IR spectra showed that the peak for the bridging  $-\text{CN}$  group was disappeared at 200 CV cycle indicating the complete electrochemical transformation of the Ni-CP into Ni-AC-1.<sup>2,19,22</sup> As the peaks for Ni-O group is observed in the 484-512  $\text{cm}^{-1}$ , it is not possible to track the change of Ni-O group using IR spectroscopy.

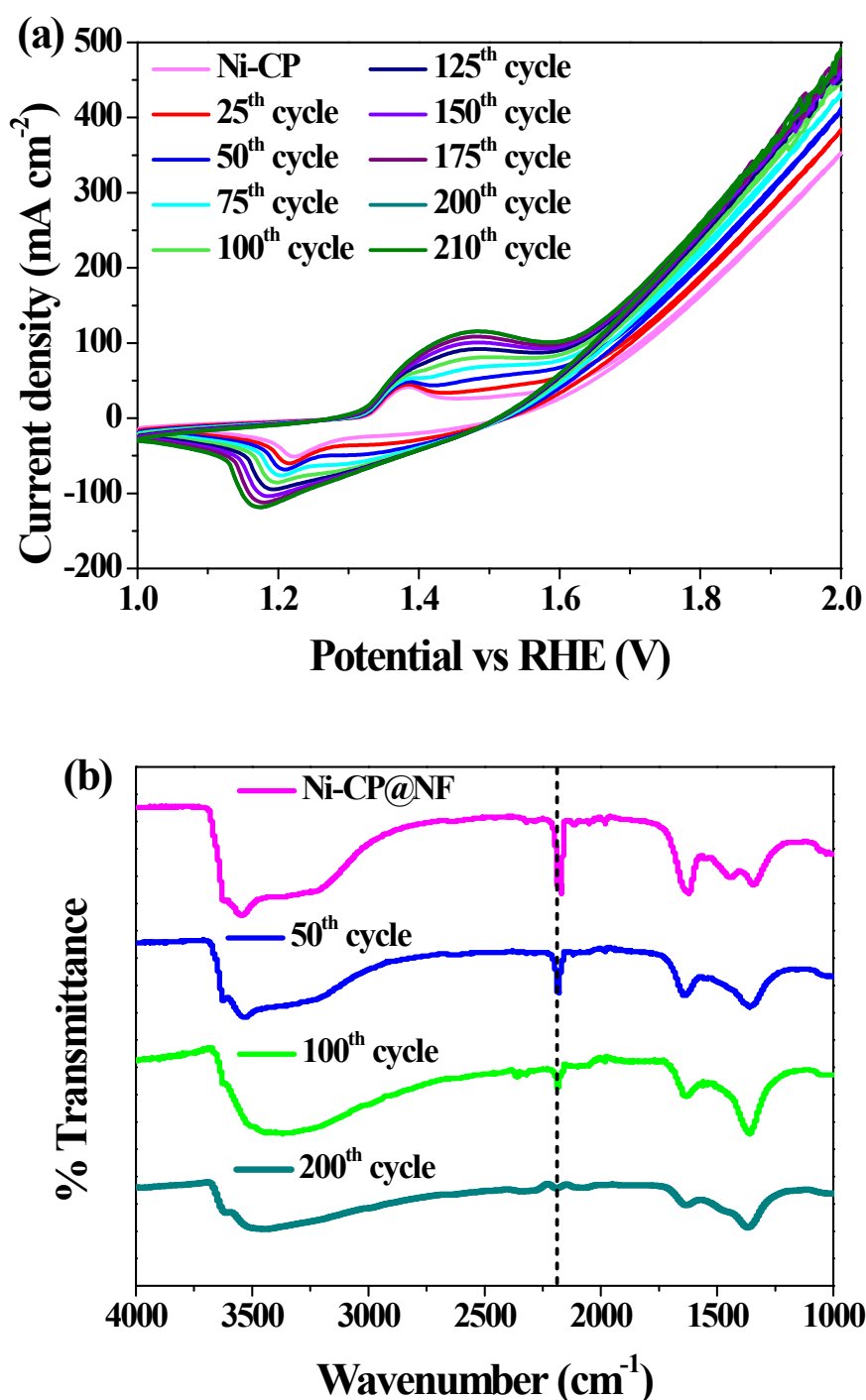


**Figure S12.** (a) CV profiles during the electrochemical activation of Ni-CP into Ni-AC-1 at, the CV profile revealed the electrochemical activation of Ni-CP for 200 CV cycles and (b) IR spectra at different CV cycles

during electrochemical reconstruction of Ni-CP into VNi-AC-1, IR spectra showed that the peak for the bridging –CN group was disappeared at 200 CV cycle indicating the complete electrochemical transformation of the Ni-CP into VNi-AC-1.<sup>2,19,22</sup>

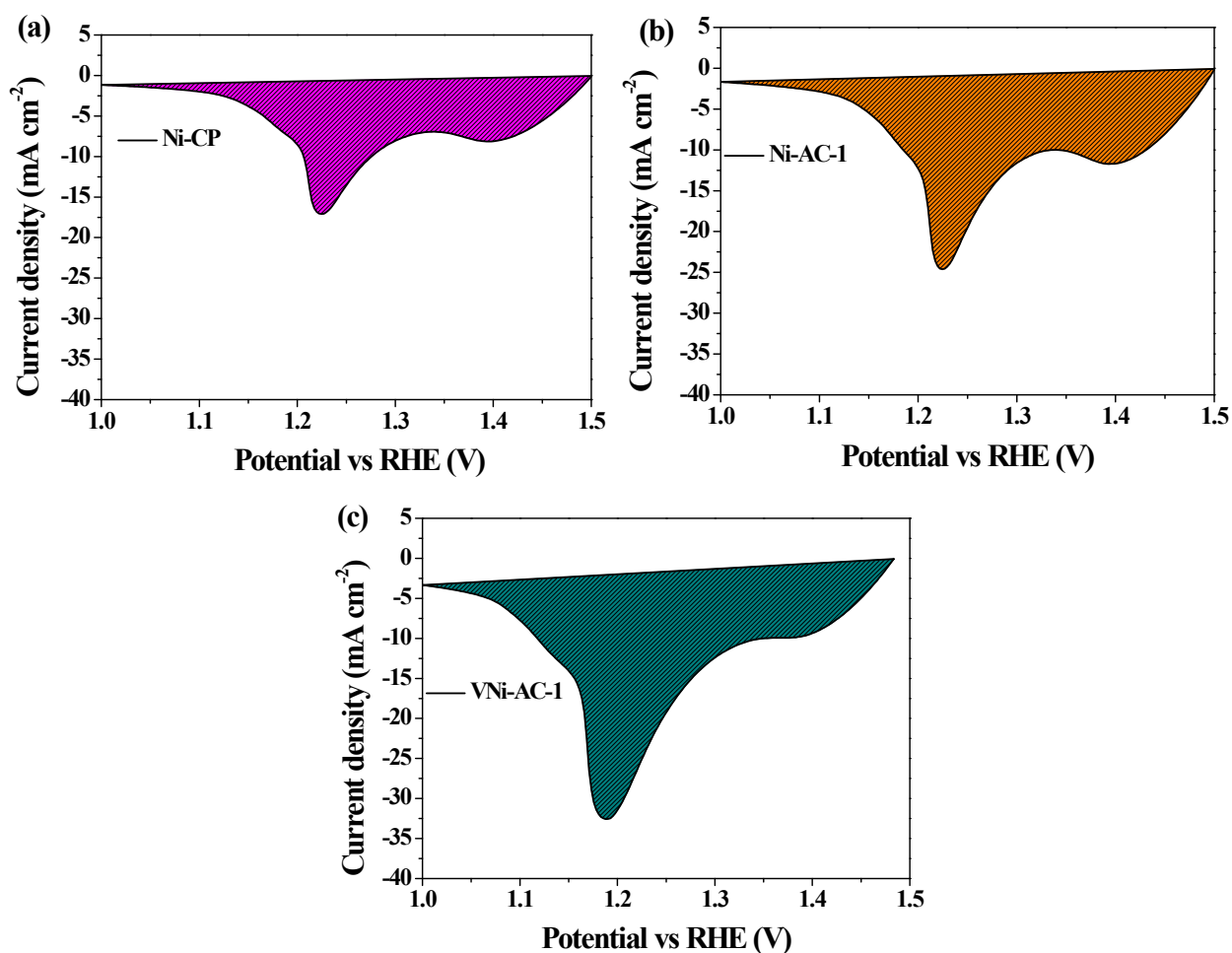


**Figure S13.** Reduction peak area of (a) Ni-CP; (b) Ni-AC-1; and (c) VNi-AC-1 used for the integration to determine the number of active sites. The electrochemical reconstruction and V-incorporation increased the area of redox peak. During the electrochemical reconstruction, Ni<sup>2+</sup> was electrochemically oxidized into Ni<sup>3+</sup> and the Ni<sup>3+</sup> was further oxidized to Ni<sup>4+</sup> under applied anodic potential. Here, the reduction peak area for the reduction of Ni<sup>4+/3+</sup> to Ni<sup>2+</sup> was integrated to calculate the number of active sites participated in the OER.<sup>23,24</sup>

**Equation S1: Determination of surface active sites using area integration of the reduction peak.**

**For Ni-CP precatalyst**

Calculated area associated with the reduction peak =  $2.8214 \times 10^{-3}$  V A

Hence the associated charge is =  $2.8214 \times 10^{-3}$  V A /  $0.002$  V s<sup>-1</sup>

$$= 1410.70 \times 10^{-3} \text{ A s}$$

$$= 1410.70 \times 10^{-3} \text{ C}$$

Now, the number of electron transferred is =  $1410.70 \times 10^{-3} \text{ C} / 1.602 \times 10^{-19} \text{ C}$

$$= 8.80 \times 10^{18}$$

Since the reduction of  $\text{Ni}^{3+}$  to  $\text{Ni}^{2+}$  is a single electron transfer reaction, the number of electrons calculated above is the same as the number of surface active sites.

Hence,

The surface-active  $\text{Ni}^{3+}$  sites participated in OER is =  **$8.80 \times 10^{18}$**

#### **For Ni-AC-1 active catalyst**

Calculated area associated with the reduction peak =  $3.9658 \times 10^{-3} \text{ V A}$

Hence the associated charge is =  $3.9658 \times 10^{-3} \text{ V A} / 0.002 \text{ V s}^{-1}$

$$= 1982.90 \times 10^{-3} \text{ A s}$$

$$= 1982.90 \times 10^{-3} \text{ C}$$

Now, the number of electron transferred is =  $1982.90 \times 10^{-3} \text{ C} / 1.602 \times 10^{-19} \text{ C}$

$$= 12.37 \times 10^{18}$$

The surface-active  $\text{Ni}^{3+}$  sites participated in OER is =  **$12.37 \times 10^{18}$**

#### **For VNi-AC-1 active catalyst**

Calculated area associated with the reduction peak =  $5.0012 \times 10^{-3} \text{ V A}$

Hence the associated charge is =  $5.0012 \times 10^{-3} \text{ V A} / 0.002 \text{ V s}^{-1}$

$$= 2500.60 \times 10^{-3} \text{ A s}$$

$$= 2500.60 \times 10^{-3} \text{ C}$$

Now, the number of electron transferred is =  $2500.60 \times 10^{-3} \text{ C} / 1.602 \times 10^{-19} \text{ C}$

$$= 15.60 \times 10^{18}$$

The surface-active  $\text{Ni}^{3+}$  sites participated in OER is =  **$15.60 \times 10^{18}$**

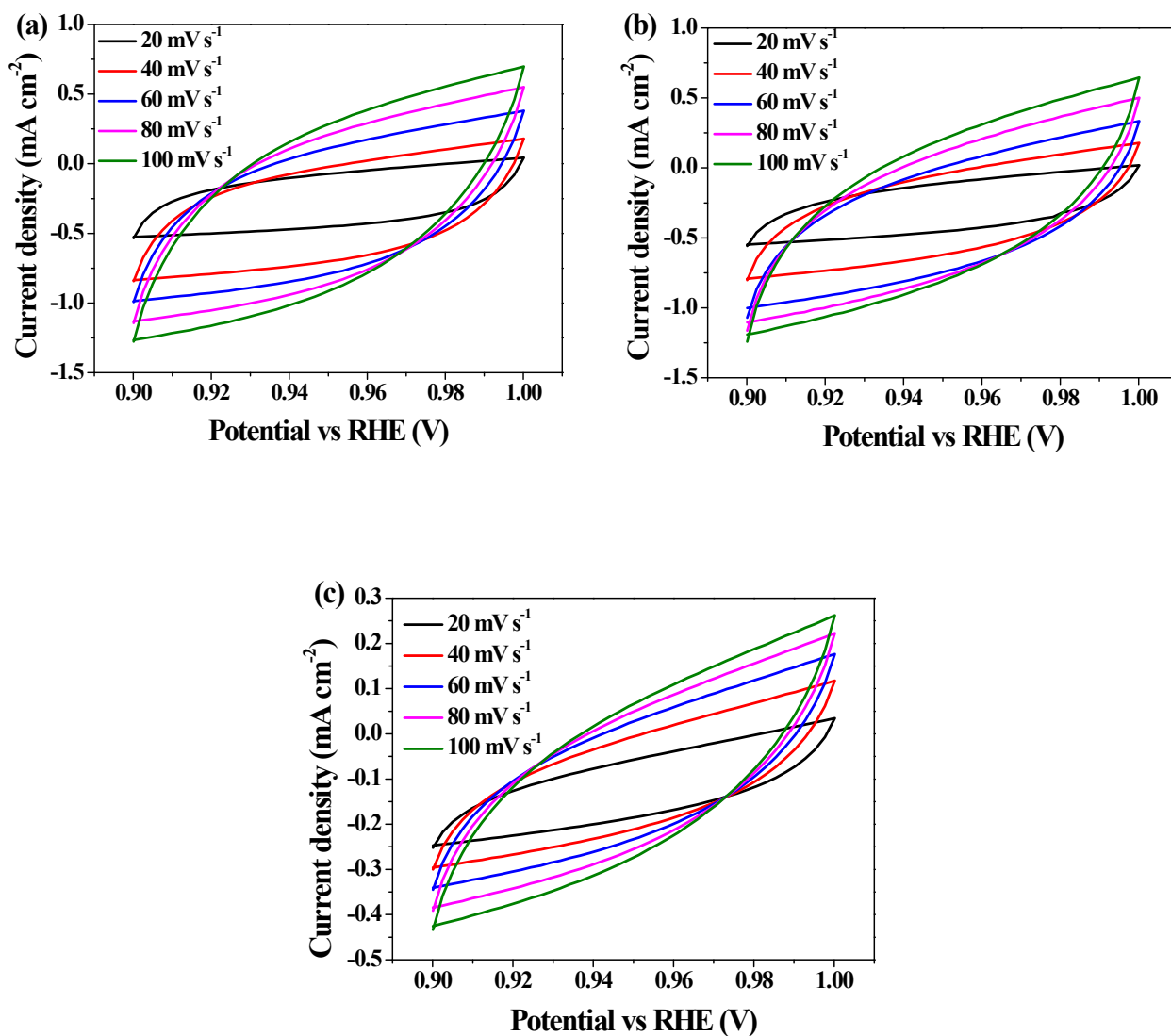


**Figure S14.** Electrochemical capacitance current determination of (a) VNi-AC-1; (b) Ni-AC-1; and (c) Ni-CP in the non-Faradaic potential range of 0.90 V to 1.00 V vs RHE with different scan rate (20, 40, 60, 80, 100 mV/s) in 1.0 M aqueous KOH solution.<sup>25</sup>

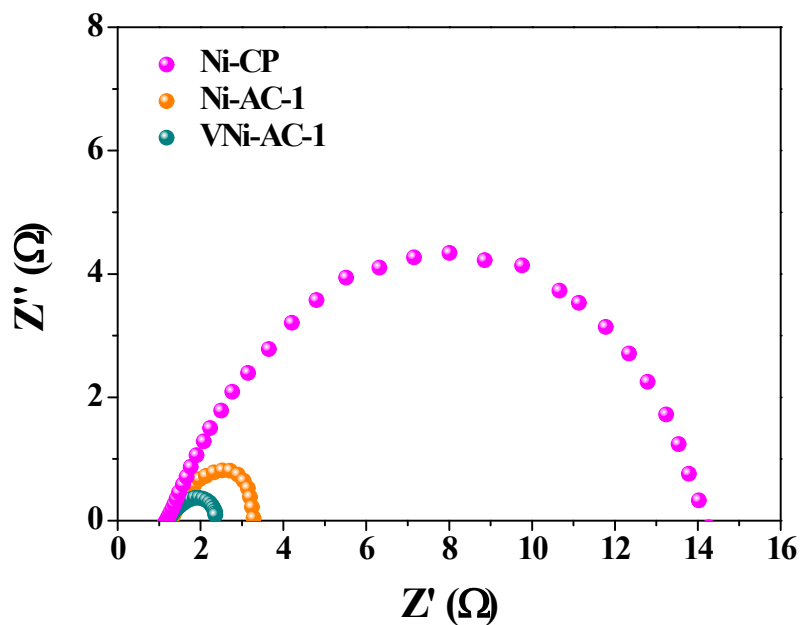


**Figure S15.** EIS spectra of Ni-CP, Ni-AC-1, and VNi-AC-1 demonstrating the lowest  $R_{ct}$  value of VNi-AC-1 (Potential = 1.50 V vs RHE). The lowest  $R_{ct}$  was ascribed to the simultaneous electrochemical reconstruction and V-incorporation.

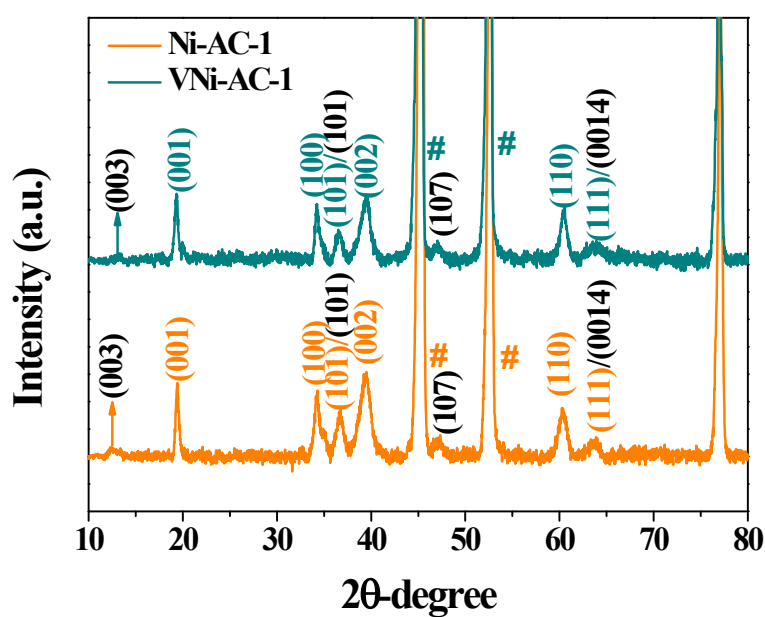


**Figure S16.** PXRD pattern of electrochemically derived Ni-AC-1 and VNi-AC-1. The PXRD peaks were well indexed and assigned for the formation of  $\beta$ -Ni(OH)<sub>2</sub> and phase  $\gamma$ -Ni(O)OH. The PXRD pattern of both catalyst

was perfectly matched with the reference pattern of the ophrasite form of  $\beta$ -Ni(OH)<sub>2</sub> having JCPDS No-14-0117 and for  $\gamma$ -Ni(O)OH (JCPDS No-06-0075). The (001) peak in VNi-AC-1 was negatively shifted by 0.12° towards lower two theta value compared to that of Ni-AC-1 ascribed to the V-introduction.<sup>26</sup> The # marked peaks were originated from the nickel foam.

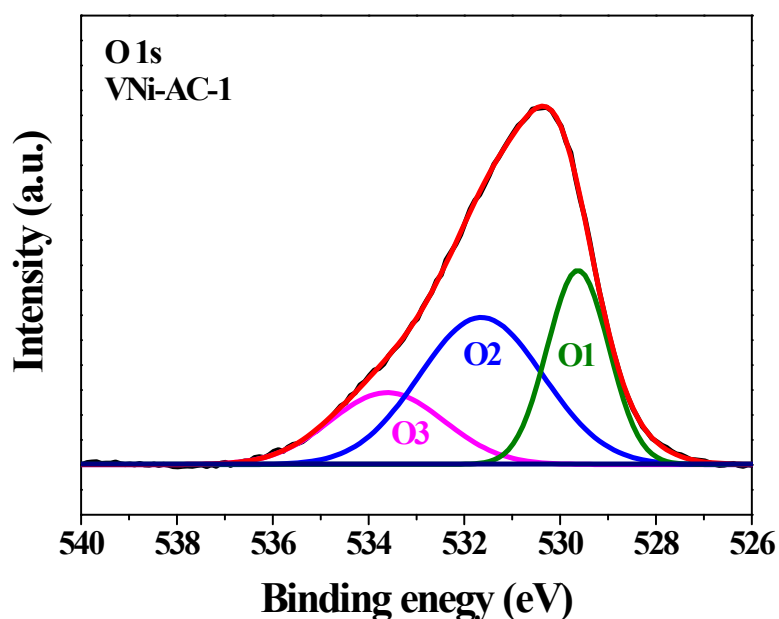


**Figure S17.** O 1s XPS of VNi-AC-1 indicating three peaks at 529.64 eV (O1), 531.66 eV (O2), and 533.62 eV attributed to the metal-oxygen bond (Ni-O), adsorbed -OH groups, and water molecules, respectively. The O2 peak VNi-AC-1 was shifted by 0.65 eV towards higher binding energy in comparison to the Ni-AC-1 ascribed to the V-introduction. The electron-withdrawing effect of V increased the binding energy of adsorbed OH in VNi-AC-1 leading to the higher affinity of Ni site for the adsorbed OH.<sup>2,19,22</sup>

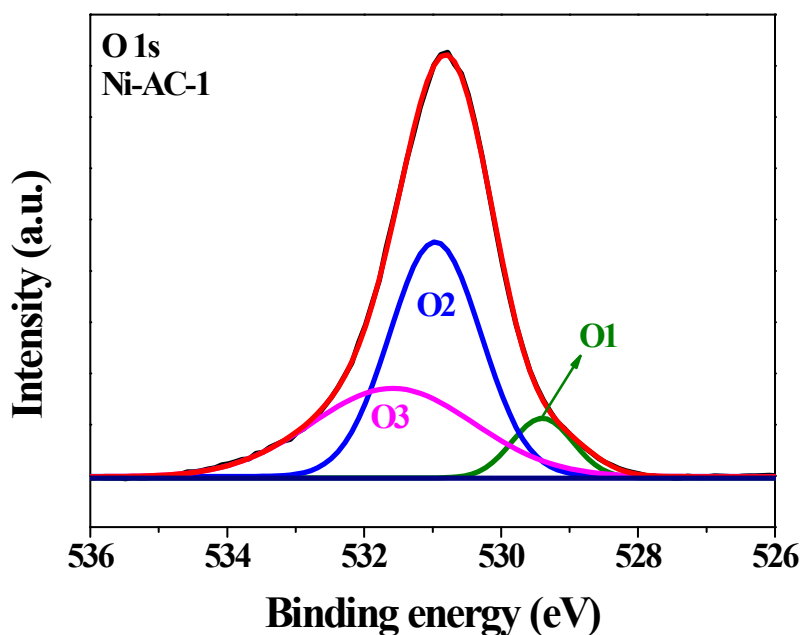


**Figure S18.** O 1s XPS of Ni-AC-1 depicting the three peaks at 529.41 eV (O1), 530.99 eV (O2), and 531.66 eV related to the metal-oxygen bond (Ni-O), adsorbed –OH groups, and water molecules, respectively.<sup>2,19,22</sup>

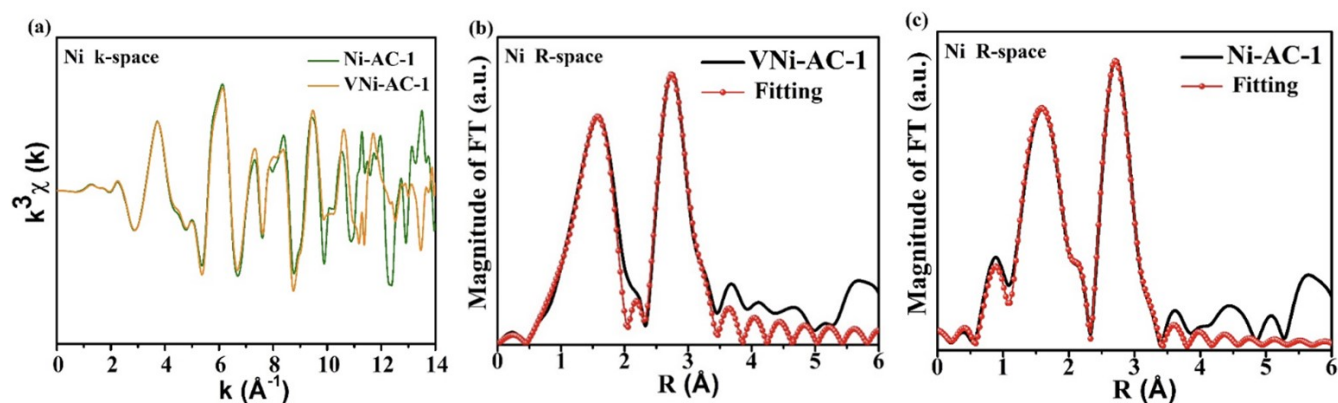


**Figure S19.** (a) Ni K EXAFS oscillation of VNi-AC-1 and Ni-AC-1; (b) FT-EXAFS spectra and fits of Ni *K*-edges of Ni-AC-1; (c) FT-EXAFS spectra and fits of Ni *K*-edges of VNi-AC-1 catalysts. The red circles represent the fitting values.<sup>27-29</sup>

**Table S3.** The details of the fitting of the EXAFS spectra showing the bond distance.

Ni	Ni-AC-1	N	$S_0^2$	CN	$\sigma^2$	$E_0$	$r_{\text{eff}}$	$\Delta R$	R(Å)
Ni-O	Path_1_[O]	6	0.949	5.69	0.01257	-9.107	2	0.04515	2.04515
Ni-Ni	Path_2_[Ni]	6	0.507	3.04	0.00606	-1.872	3.1	0.02220	3.12220
Ni	VNi-AC-1	N	$S_0^2$	CN	$\sigma^2$	$E_0$	$r_{\text{eff}}$	$\Delta R$	R(Å)
Ni-O	Path_1_[O]	6	0.857	5.14	0.00555	-6.661	2	0.04378	2.04378
Ni-Ni	Path_3_[Ni]	6	0.533	3.19	0.00662	-6.222	3.1	-0.00629	3.09361

Where CN is the actual coordination number. The CN value is determined by multiplying the amplitude reduction factor ( $S_0^2$ ) with ideal coordination number N,  $S_0^2$  is amplitude reduction factor, R is the interatomic distance (the bond length between X-ray absorbing atoms and surrounding coordination atoms);  $\sigma^2$  is Debye-

Waller factor (a measure of thermal and static disorder in absorber-scatterer distances);  $E_0$ , inner potential correction; R-factor, indicates the goodness of the fit.

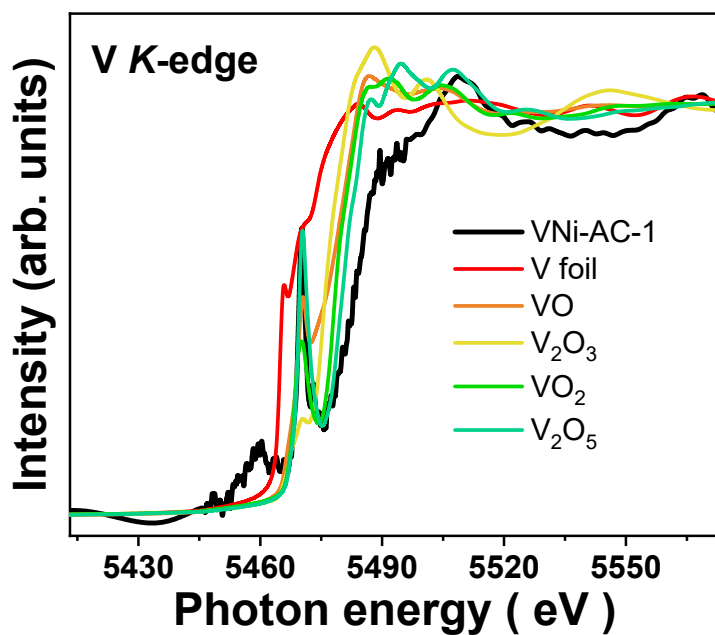
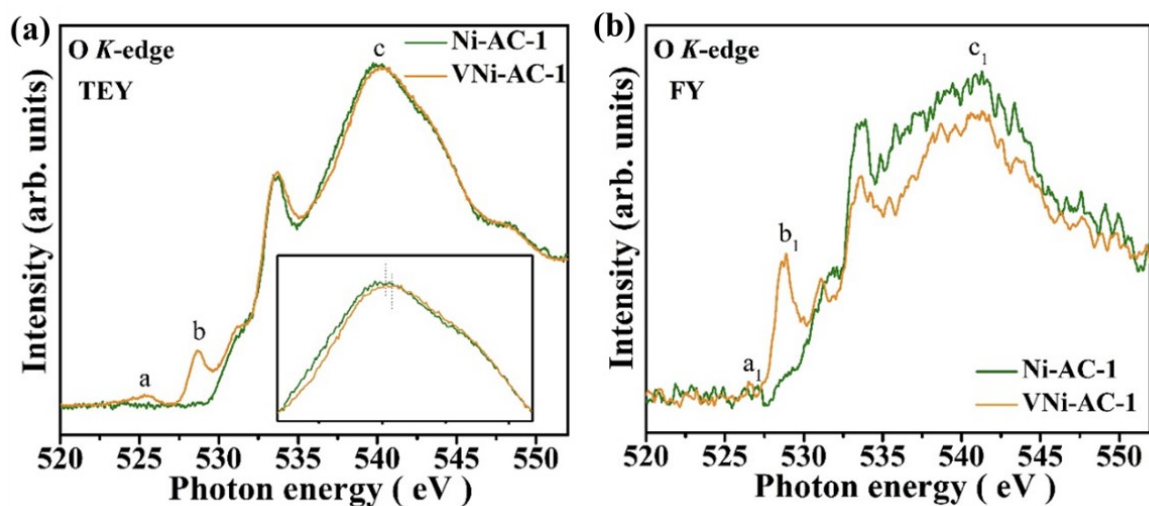
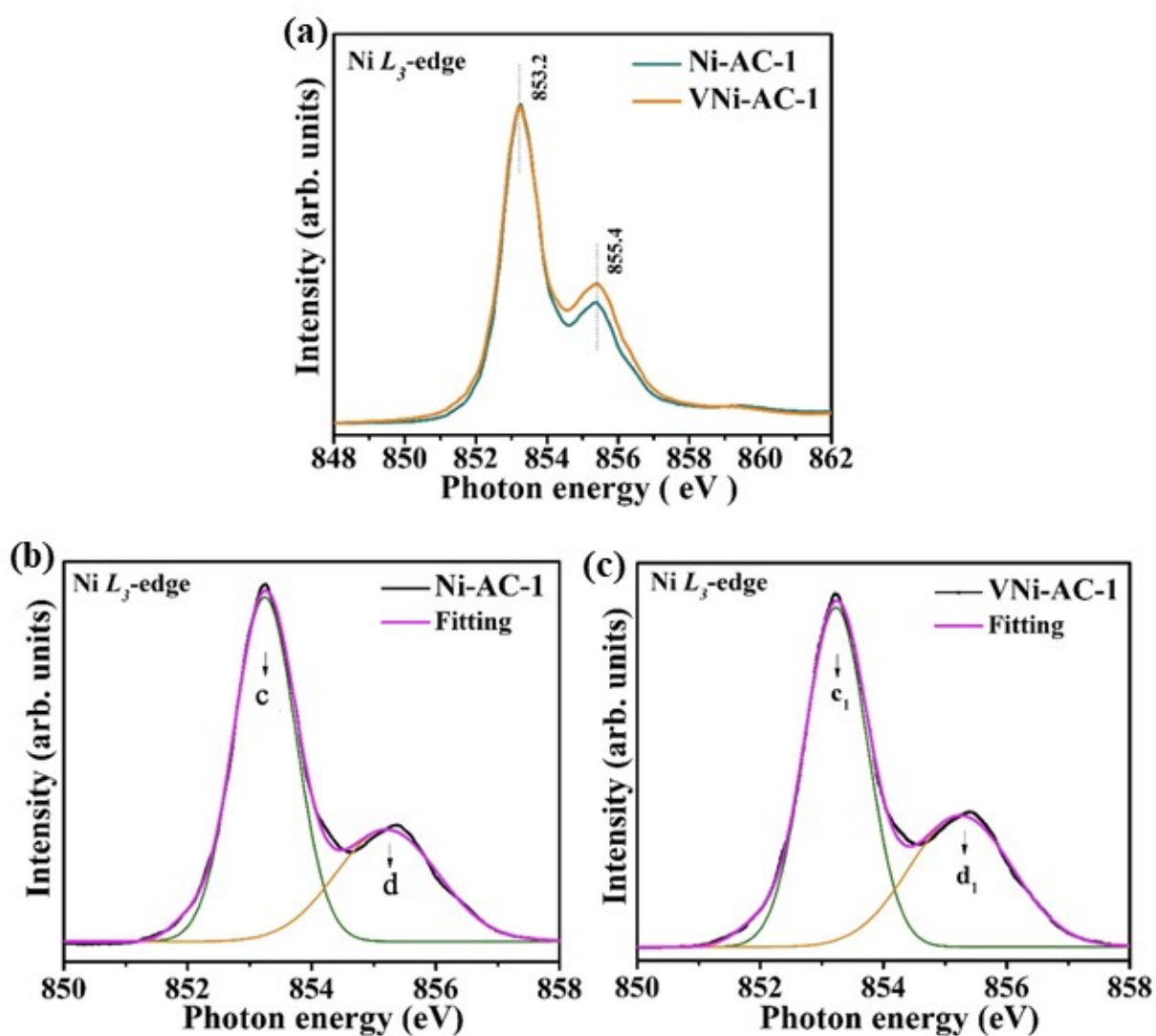


Figure S20. V K edge XANES spectra of VNi-AC-1 compared with V foil, VO, VO<sub>2</sub>, V<sub>2</sub>O<sub>3</sub> and V<sub>2</sub>O<sub>5</sub>.



**Figure S21.** (a) O K-edge spectra of VNi-AC-1 and Ni-AC-1 in TEY and (b) O K-edge spectra of VNi-AC-1 and Ni-AC-1 in FY mode.<sup>30-34</sup>



**Figure S22.** (a) Ni  $L$ -edge spectra of VNi-AC-1 and Ni-AC-1; (b) (a) fitted Ni  $L$ -edge spectra of Ni-AC-1 and (c) fitted Ni  $L$ -edge spectra of VNi-AC-1.<sup>35-37</sup>

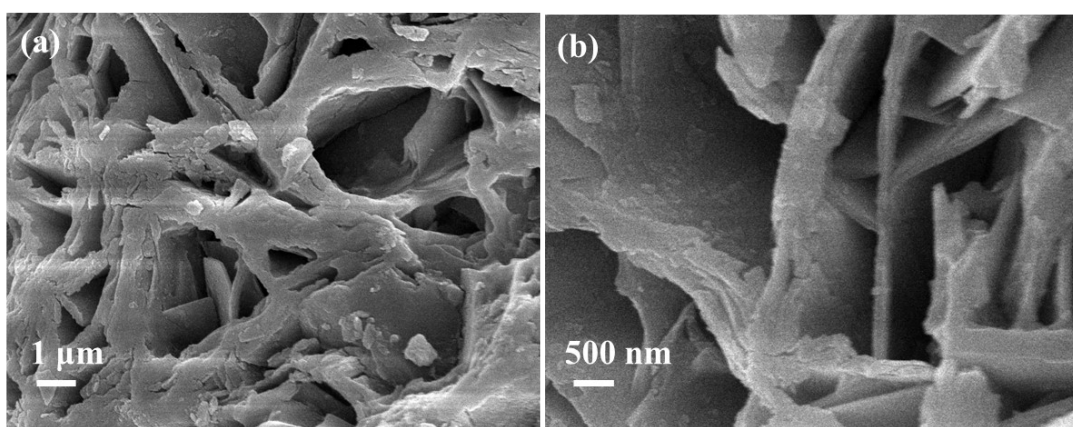


**Figure S23.** SEM image of electrochemically derived Ni-AC-1.

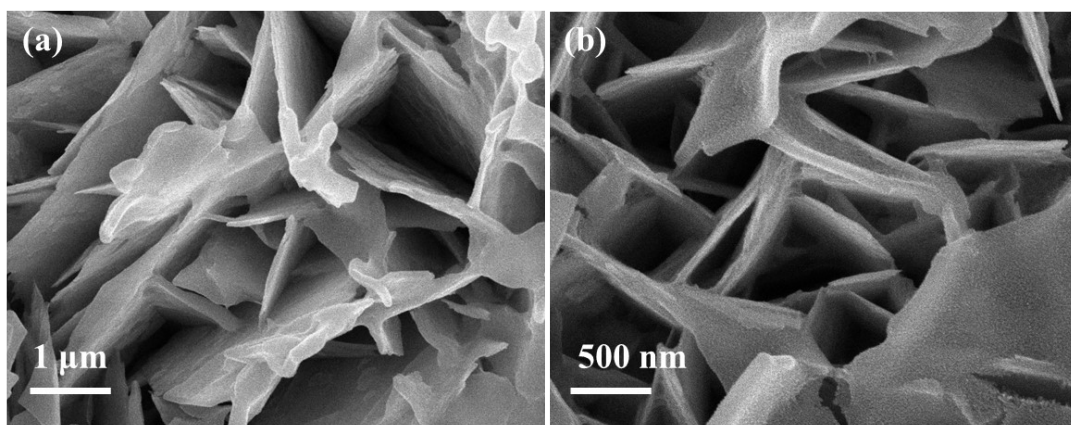


**Figure S24.** (a-b) SEM image of electrochemically derived VNi-AC-1.

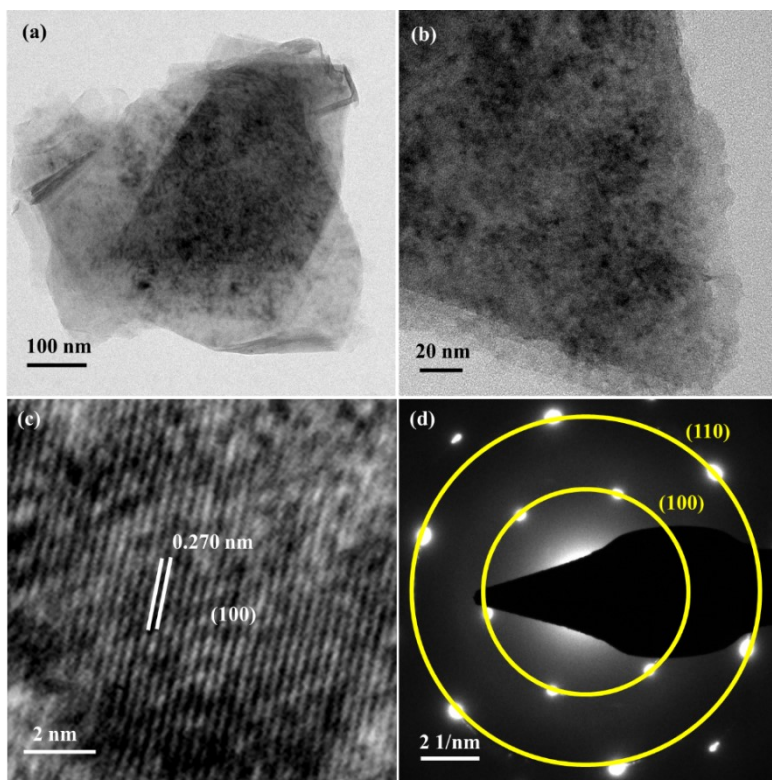


**Figure S25.** (a-b) TEM images of electrochemically derived Ni-AC-1 at different resolutions showing the ultrathin nanosheet morphology; (c) HRTEM image of Ni-AC-1 signifying the d-spacing of 0.270 nm attributed to the (100) plane of  $\beta$ -Ni(OH)<sub>2</sub> (JCPDS No-14-0117) or  $\gamma$ -Ni(O)OH (JCPDS No-06-0075); and (d) corresponding SAED pattern indexed for the (100) and (110) planes of  $\beta$ -Ni(OH)<sub>2</sub>.

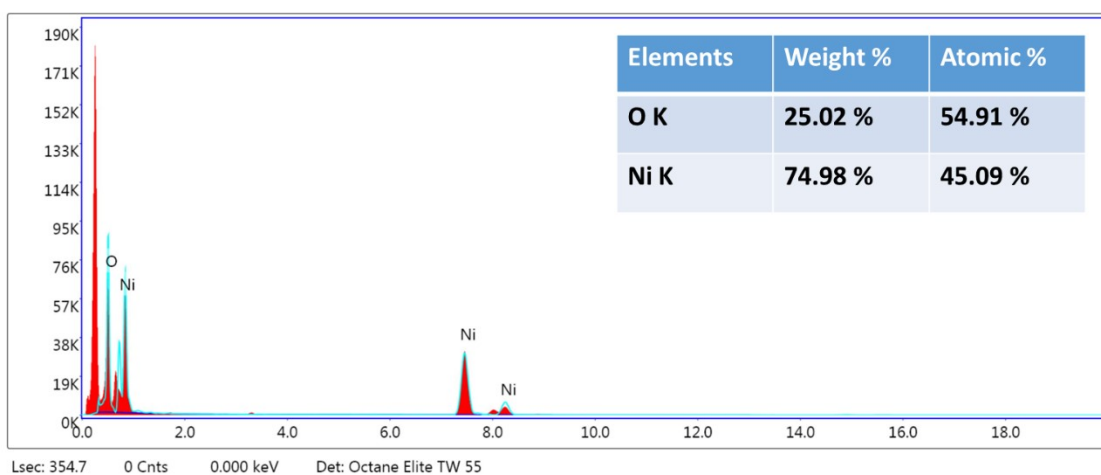


**Figure S26.** EDX spectrum of electrochemically derived Ni-AC-1 showing the existence of Ni and O elements.

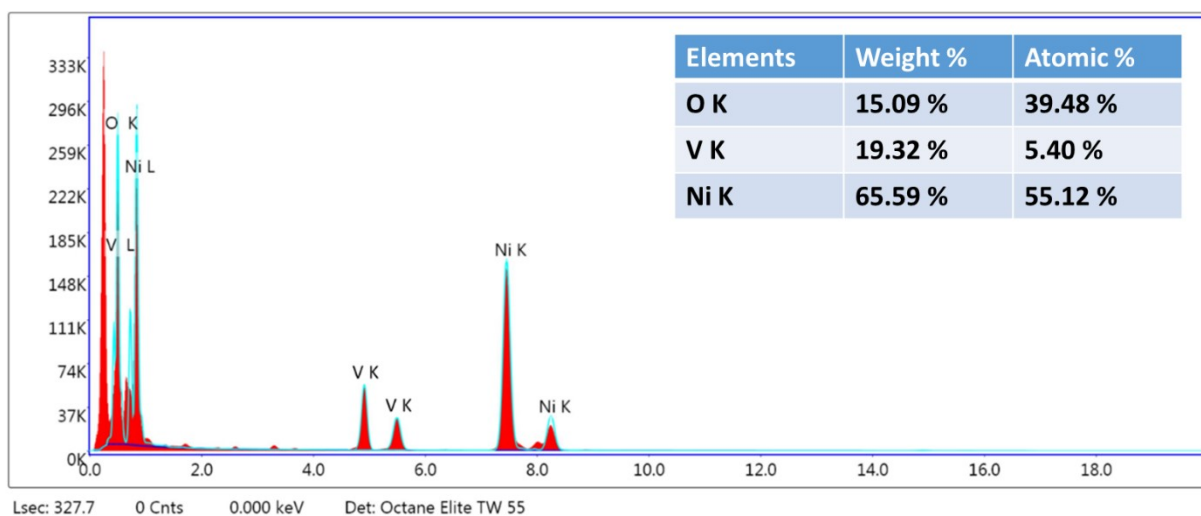


**Figure S27.** EDX spectrum of electrochemically derived VNi-AC-1 showing the existence of Ni, V, and O elements.

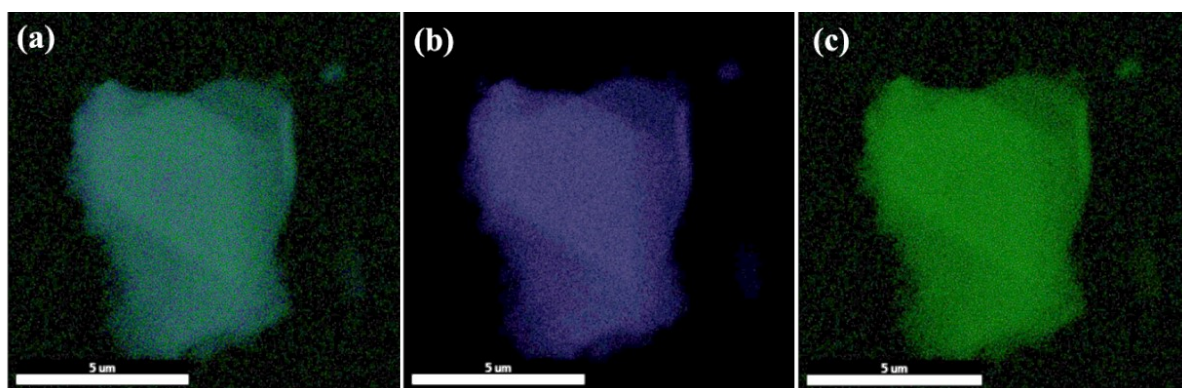


**Figure S28.** Elemental mapping images of (a) overlapping image; (b) Ni; and (c) O in Ni-AC-1.

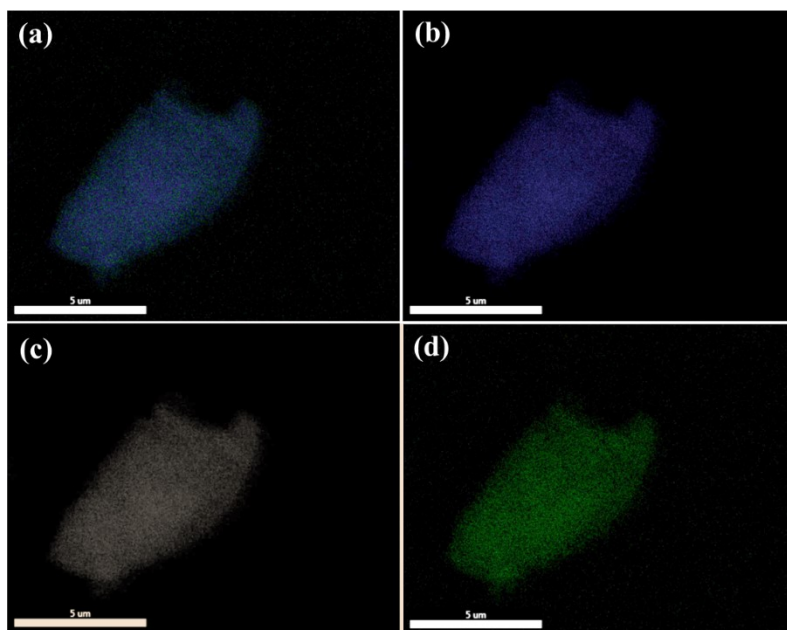


**Figure S29.** Elemental mapping images of (a) overlapping; (b) Ni; (c) V; and (d) O in VNi-AC-1.

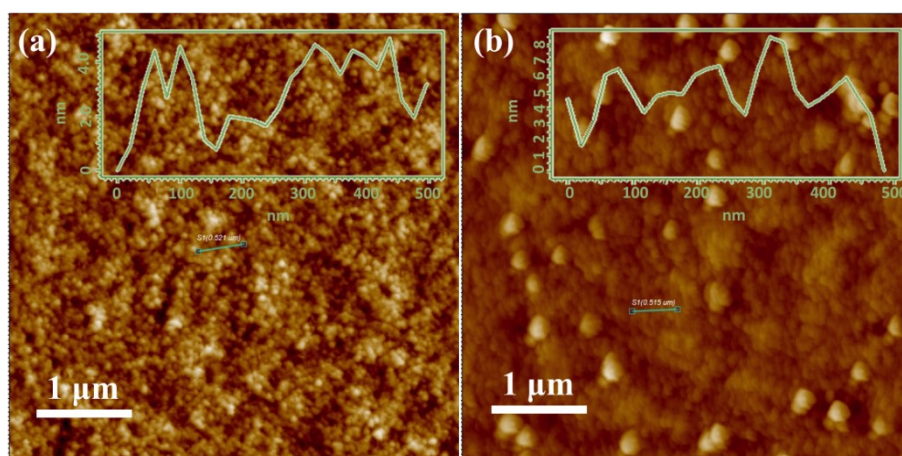


**Figure S30.** (a) AFM image of VNi-AC-1 and corresponding height profile inset displaying the 3-4 nm average thickness of the ultrathin VNi-AC-1 nanosheets; (b) AFM image of Ni-AC-1; and corresponding height profile inset indicating the 6-8 nm average thickness of the ultrathin Ni-AC-1 nanosheets.

**Table S4.** Comparison of the alkaline water oxidation activities of synthesized catalysts with literature-reported catalysts.

Catalyst	Electrolyte	Current density (mA/cm <sup>2</sup> )	Overpotential (mV)	References
<b>(a) Our catalysts</b>				
VNiAC-1 <b>work</b>	1.0 M aqueous KOH	50	290	<b>This</b>
VNiAC-2 <b>work</b>	1.0 M aqueous KOH	50	320	<b>This</b>
VNiAC-3 <b>work</b>	1.0 M aqueous KOH	50	305	<b>This</b>
VNiAC-4 <b>work</b>	1.0 M aqueous KOH	50	335	<b>This</b>
<b>(b) PBA derived catalysts</b>				
NiCoO <sub>x</sub>	1.0 M aqueous KOH	10	380	38
NiFeP	1.0 M aqueous KOH	10	290	39
NiCoSe <sub>2</sub>	1.0 M aqueous KOH	10	320	40
NiCo-Oxide	1.0 M aqueous KOH	10	280	41
NiFe@C	1.0 M aqueous KOH	10	280	42
Ni <sub>x</sub> P <sub>y</sub>	1.0 M aqueous KOH	10	300	43
NiCoFeS	1.0 M aqueous KOH	10	320	44
<b>(c) Self-supported catalysts</b>				
NiO@NF	1.0 M aqueous KOH	10	422	45
NiP@NF	1.0 M aqueous KOH	10	335	46
NiO@NF	1.0 M aqueous KOH	10	390	47
(Ni,Co) <sub>0.85</sub> Se@CC	1.0 M aqueous KOH	10	300	48
NiFeSe@NiSe/O@C	1.0 M aqueous KOH	10	270	49
NiSe@NiOOH@NF	1.0 M aqueous KOH	50	332	50
<b>(d) Ultrathin layered double hydroxide nanosheets</b>				
NiV-LDH	1.0 M aqueous KOH	27	350	51
NiV-LDH	1.0 M aqueous KOH	57	350	52
NiV-LDH	1.0 M aqueous KOH	10	200	53
NiFeV-LDH	1.0 M aqueous KOH	20	260	54
NiCoV-LDH	1.0 M aqueous KOH	10	280	55
NiV-LDH	1.0 M aqueous KOH	26	10	56

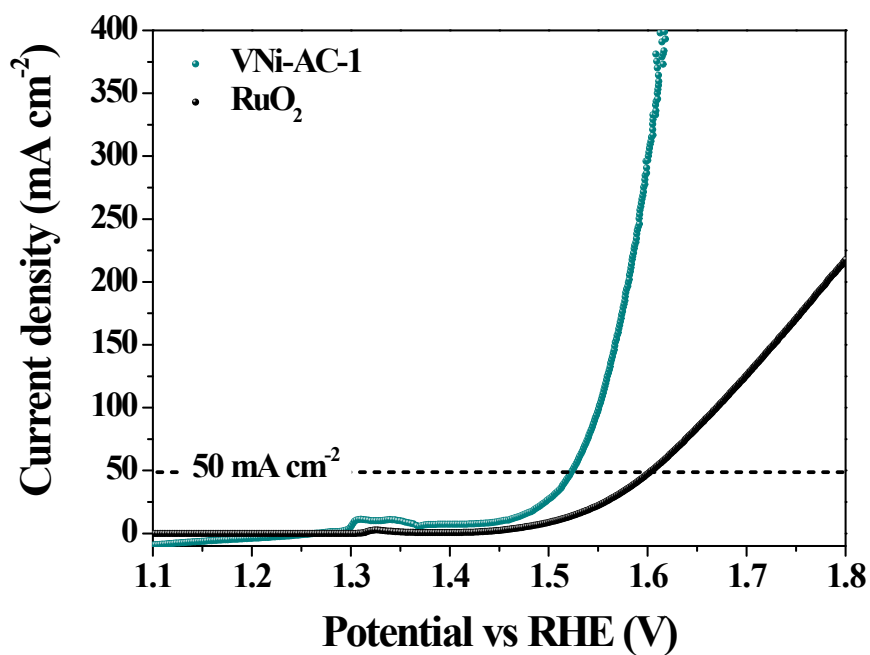


**Figure S31.** LSV profile for the oxygen evolution reaction of VNi-AC-1 compared with the noble metal based RuO<sub>2</sub> catalyst showing the best OER activity of electrochemically derived VNi-AC-1.

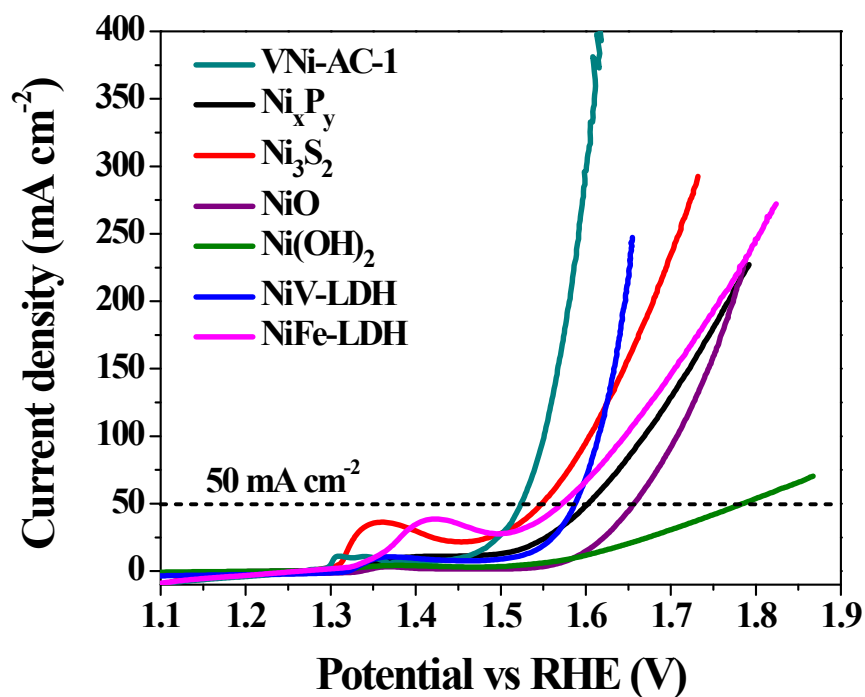


**Figure S32.** LSV profiles for the oxygen evolution reaction of VNi-AC-1 compared with Ni-based NiFe-LDH, NiV-LDH, Ni(OH)<sub>2</sub>, NiO, Ni<sub>x</sub>P<sub>y</sub> and Ni<sub>3</sub>S<sub>2</sub> showing the best OER activity of electrochemically derived VNi-AC-1.

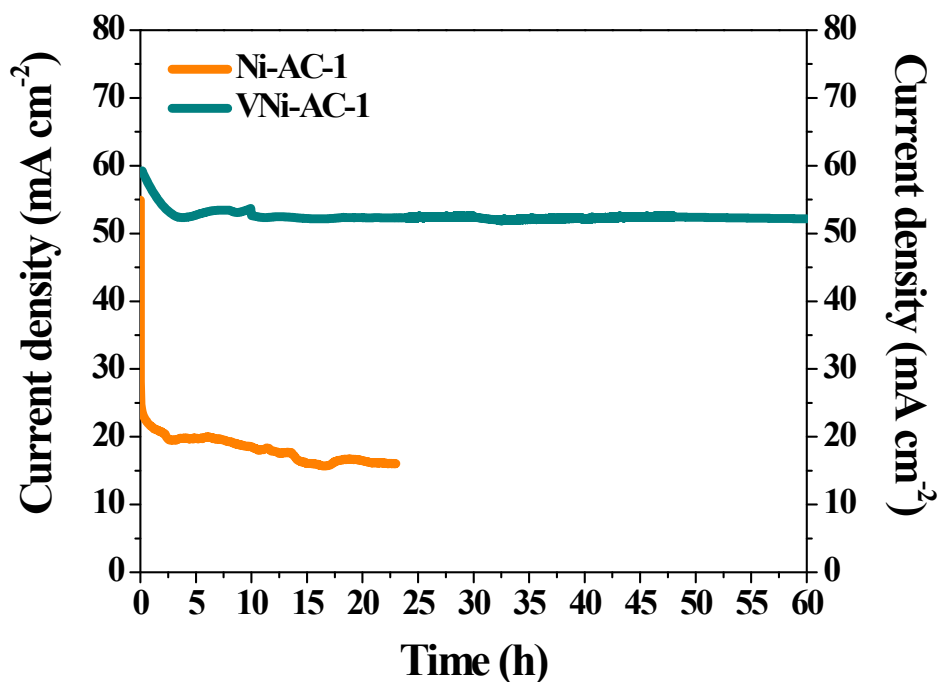


**Figure S33.** Chronoamperometric measurement for the oxygen evolution reaction of VNi-AC-1 and Ni-AC-1 at 1.53 V vs RHE. The current density of Ni-AC-1 was decreased after 10 h due to the deactivation while VNi-AC-1 showed the enhanced stability for 60 h.

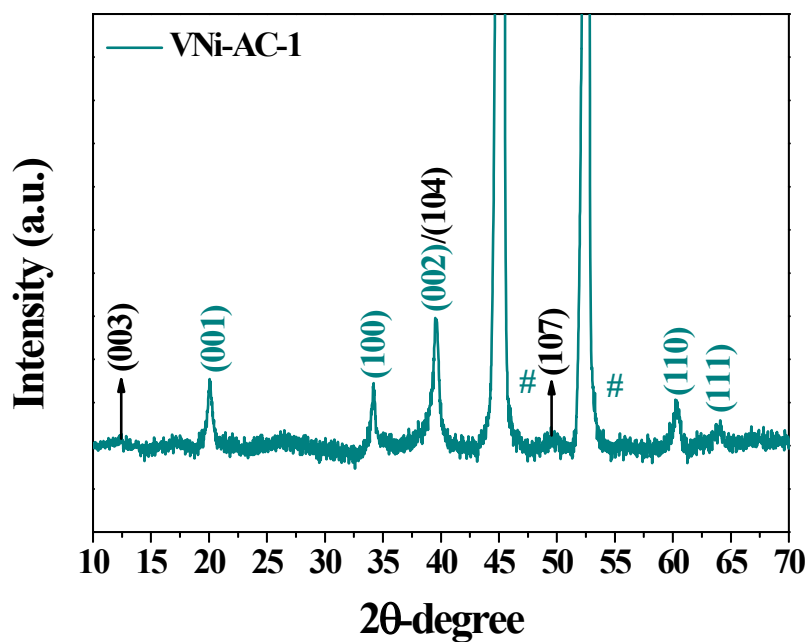


**Figure S34.** PXRD pattern of VNi-AC-1 after the 60 h OER CA demonstrating that the crystal structure was retained after 60 h CA matching with  $\beta$ -Ni(OH)<sub>2</sub> (JCPDS No-14-0117) and  $\gamma$ -Ni(O)OH (JCPDS No-06-0075).<sup>26</sup>

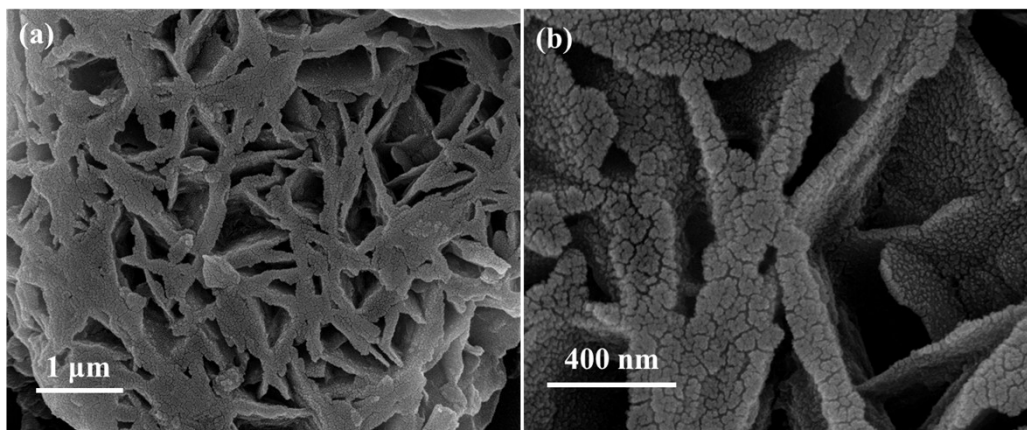


**Figure S35.** (a-b) SEM images of VNi-AC-1 at different resolutions presenting the ultrathin nanosheet like morphology after 60 h OER CA.

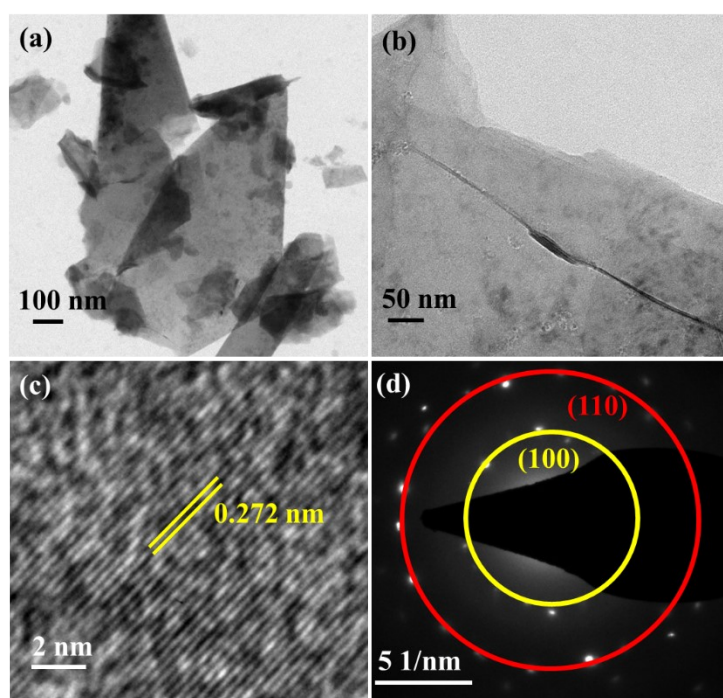


**Figure S36.** (a-b) TEM images of VNi-AC-1 at different resolutions indicating the ultrathin nanosheet like morphology after 60 h OER CA; (c) corresponding HRTEM image detecting the lattice spacing of 0.272 nm for the (100) plane of  $\beta$ -Ni(OH)<sub>2</sub> (JCPDS No-14-0117); (d) SAED pattern indexed for the (100) and (110) planes of the  $\beta$ -Ni(OH)<sub>2</sub> (JCPDS No-14-0117).

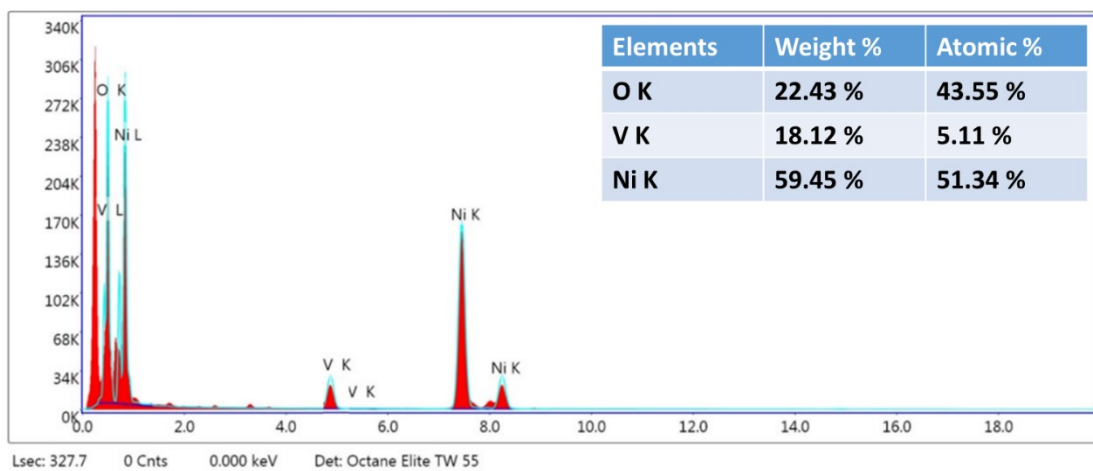


**Figure S37.** EDX spectrum of VNi-AC-1 after 60 h OER CA showing the presence of V, Ni, C and O elements.

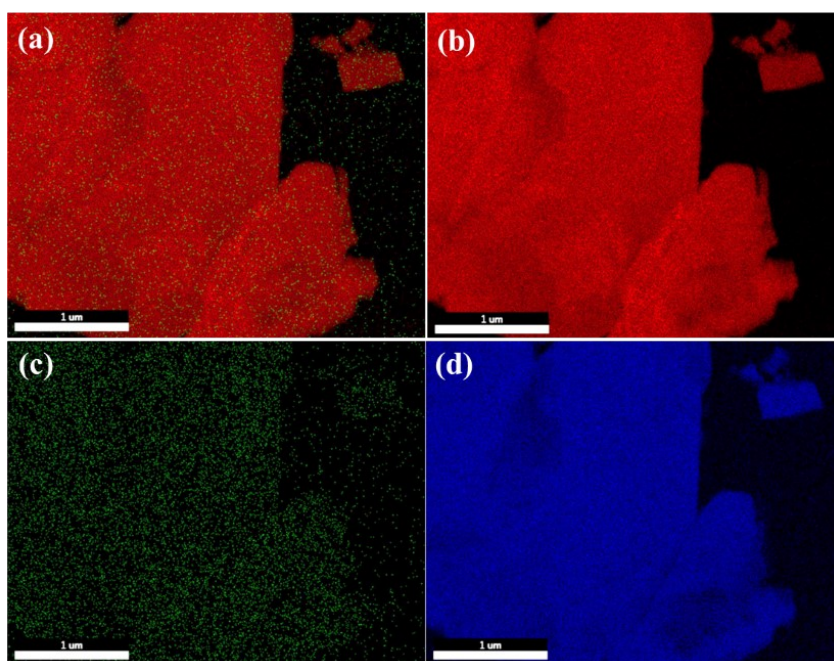


**Figure S38.** EDX elemental mapping of VNi-AC-1 after 60 h OER CA showing the presence of (a) overlapping; (b) Ni; (c) V; and (d) O elements.

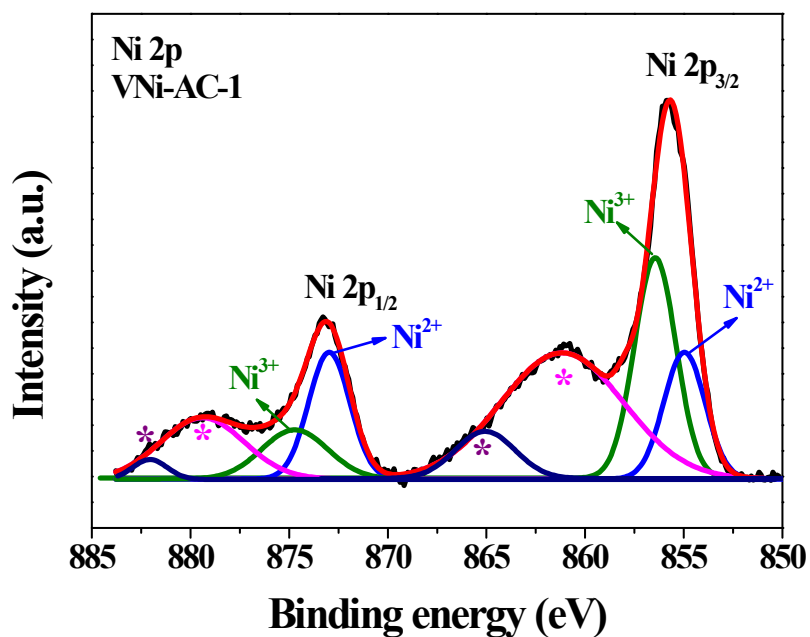


**Figure S39.** Ni 2p XPS of VNi-AC-1 after 60 h OER-CA. The spectrum depicted two peaks at 855.67 eV and 873.17 eV assigned to the Ni 2p<sub>3/2</sub> and Ni 2p<sub>1/2</sub>, respectively. The peaks at 855.03 eV and 856.45 eV were attributed to the Ni<sup>2+</sup> and Ni<sup>3+</sup>, respectively. The \* marked peaks were assigned for the satellite peak.<sup>20,21</sup>

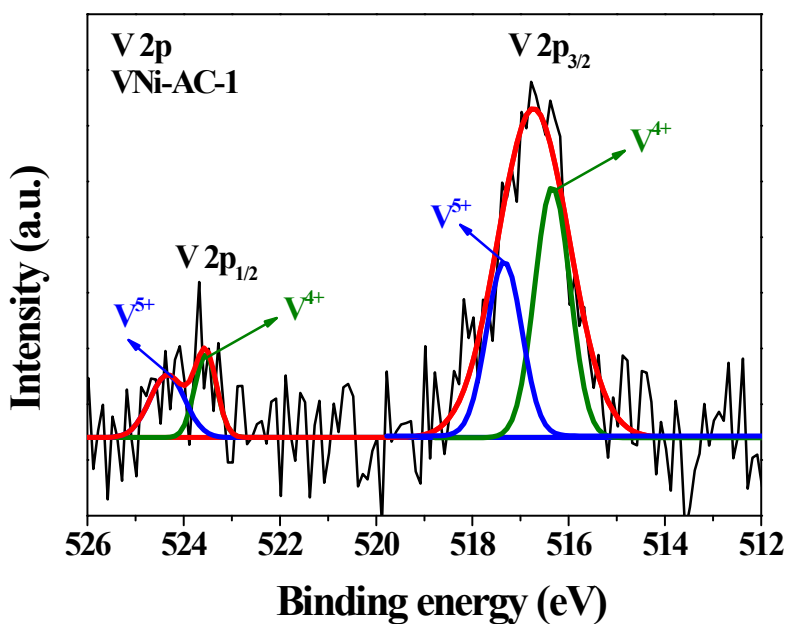


**Figure S40.** V 2p XPS of VNi-AC-1 after 60 h OER-CA. The two peaks at 516.72 eV and 523.69 eV were appeared for the V 2p<sub>3/2</sub> and V 2p<sub>1/2</sub>, respectively. The peaks at 516.35 eV and 517.32 eV were observed for the V<sup>4+</sup> and V<sup>5+</sup>, respectively. The \* marked peaks were assigned for the satellite peak.<sup>57,58</sup>

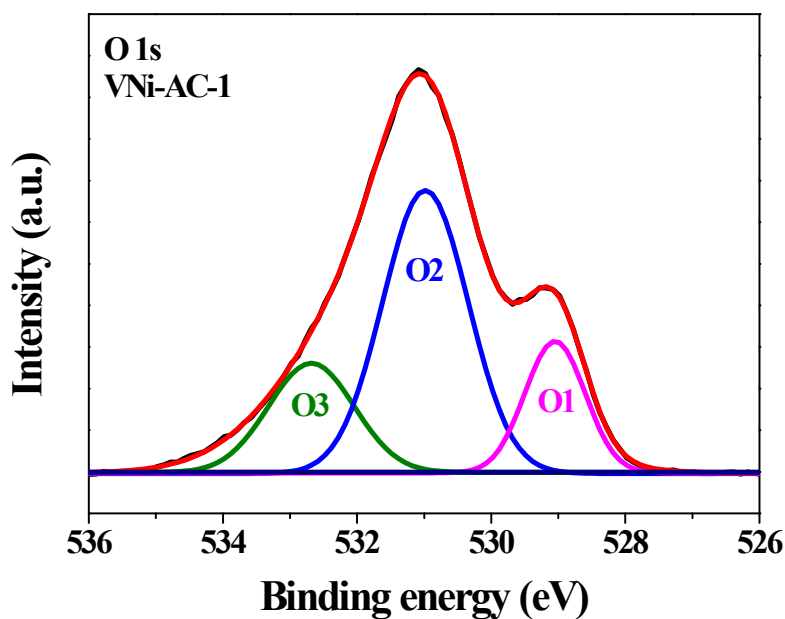


**Figure S41.** O 1s XPS of VNi-AC-1 after 60 h OER-CA. The three peaks at 529.06 eV (O1), 530.99 eV (O2), and 532.70 eV (O3) were originated, which were related to the metal-oxygen bond (Ni-O), adsorbed -OH, and associated water molecules, respectively.<sup>19,57</sup>

## References

- [1] S. Dutta, A. Indra, Y. Feng, T. Song and U. Paik, *ACS Appl. Mater. Interfaces*, 2017, **9**, 33766–33774.
- [2] A. Indra, U. Paik and T. Song, *Angew. Chem. Int. Ed.*, 2018, **57**, 1241–1245.
- [3] J. M. P. Martirez and E. A. Carter, *J. Am. Chem. Soc.*, 2019, **141**, 693–705.
- [4] G. Kresse and J. Furthmüller, *Phys. Rev. B*, 1996, **54**, 11169–11186.
- [5] G. Kresse and J. Furthmüller, *Comput. Mater. Sci.*, 1996, **6**, 15–50.
- [6] J. P. Perdew, K. Burke and M. Ernzerhof, *Phys. Rev. Lett.*, 1996, **77**, 3865–3868.
- [7] S. Grimme, *J. Comput. Chem.*, 2004, **25**, 1463–1473.
- [8] S. Grimme, *J. Comput. Chem.*, 2006, **27**, 1787–1799.
- [9] H. J. Monkhorst and J. D. Pack, *Phys. Rev. B*, 1976, **13**, 5188–5192.
- [10] K. Mathew, R. Sundararaman, K. Letchworth-Weaver, T. A. Arias and R. G. Hennig, *J. Chem. Phys.*, 2014, **140**, 0–8.
- [11] K. Mathew, V. S. C. Kolluru, S. Mula, S. N. Steinmann and R. G. Hennig, *J. Chem. Phys.*, 2019, **151**, 234101.
- [12] A. S. Lileev, D. V Loginova and A. K. Lyashchenko, *Russ. J. Inorg. Chem.*, 2011, **56**, 961–967.
- [13] J. K. Nørskov, J. Rossmeisl, A. Logadottir, L. Lindqvist, J. R. Kitchin, T. Bligaard and H. Jónsson, *J. Phys. Chem. B*, 2004, **108**, 17886–17892.
- [14] I. C. Man, H.-Y. Su, F. Calle-Vallejo, H. A. Hansen, J. I. Martínez, N. G. Inoglu, J. Kitchin, T. F. Jaramillo, J. K. Nørskov and J. Rossmeisl, *ChemCatChem*, 2011, **3**, 1159–1165.
- [15] Q. Liang, G. Brocks and A. Bieberle-Hütter, *J. Phys. Energy*, 2021, **3**, 26001.

- [16] M. Hu, S. Ishihara and Y. Yamauchi, *Angew. Chem. Int. Ed.*, 2013, **125**, 1273–1277.
- [17] R. Lu, Y. Chen, H. Zhou and A. Yuan, *Acta Chim. Sin.*, 2010, **68**, 1199–1204.
- [18] E. Ruiz, S. Alvarez, R. Hoffmann and J. Bernstein, *J. Am. Chem. Soc.*, 1994, **116**, 8207–8221.
- [19] B. Singh, O. Prakash, P. Maiti, P. W. Menezes and A. Indra, *Chem. Commun.*, 2020, **56**, 15036–15039.
- [20] P. W. Menezes, A. Indra, C. Das, C. Walter, C. Göbel, V. Gutkin, D. Schmeißer and M. Driess, *ACS Catal.*, 2016, **7**, 103–109.
- [21] S. Dutta, A. Indra, Y. Feng, T. Song and U. Paik, *ACS Appl. Mater. Interfaces*, 2017, **9**, 33766–33774.
- [22] B. Singh, O. Prakash, P. Maiti and A. Indra, *ACS Appl. Nano Mater.*, 2020, **3**, 6693–6701.
- [23] S. Anantharaj and S. Kundu, *ACS Energy Lett.*, 2019, **4**, 1260–1264.
- [24] S. Anantharaj, S. R. Ede, K. Karthick, S. Sam Sankar, K. Sangeetha, P. E. Karthik and S. Kundu, *Energy Environ. Sci.*, 2018, **11**, 744–771.
- [25] P. W. Menezes, A. Indra, I. Zaharieva, C. Walter, S. Loos, S. Hoffmann, R. Schlögl, H. Dau and M. Driess, *Energy Environ. Sci.*, 2019, **12**, 988–999.
- [26] S. Anantharaj, P. E. Karthik and S. Kundu, *Catal. Sci. Technol.*, 2017, **7**, 882–893.
- [27] U. P. Gawai, S. D. Kamble, S. K. Gurav, M. N. Singh, A. K. Yadav, S. N. Jha, N. P. Lalla, M. R. Bodke, M. D. Shirsat and B. N. Dole, *ACS Omega*, 2022, **7**, 6700–6709.
- [28] W. Liu, Y. Chen, H. Qi, L. Zhang, W. Yan, X. Liu, X. Yang, S. Miao, W. Wang, C. Liu, A. Wang, J. Li and T. Zhang, *Angew. Chem. Int. Ed.*, 2018, **130**, 7189–7193.
- [29] H. Lei, L. Ma, Q. Wan, S. Tan, B. Yang, Z. Wang, W. Mai and H. J. Fan, *Adv. Energy Mater.*, 2022, **12**, 2202522.
- [30] S. Li, N. Sharma, C. Yu, Y. Zhang, G. Wan, R. Fu, H. Huang, X. Sun, S. -J. Lee, J. -S. Lee, D. Nordlund, P. Pianetta, K. Zhao, Y. Liu and J. Qiu, *Adv. Mater.*, 2020, **33**, 2006147.
- [31] J. Yang, C. Yu, C. Hu, M. Wang, S. Li, H. Huang, K. Bustillo, X. Han, C. Zhao, W. Guo, Z. Zeng, H. Zheng and J. Qiu, *Adv. Funct. Mater.*, 2018, **21**, 1803272.
- [32] H. Sun, L. Li, H.-C. Chen, D. Duan, M. Humayun, Y. Qiu, X. Zhang, X. Ao, Y. Wu, Y. Pang, K. Huo, C. Wang and Y. Xiong, *Sci. Bull.*, 2022, **67**, 1763–1775.
- [33] D. Maganas, M. Roemelt, M. Havecker, A. Trunschke, A. Knop-Gericke, R. Schlogl and F. Neese, *Phys. Chem. Chem. Phys.*, 2013, **15**, 7260–7276.
- [34] Y. Ren, J. Oyama, T. Uchiyama, Y. Orikasa, T. Watanabe, K. Yamamoto, T. Takami, Y. Nishiki, S. Mitsushima and Y. Uchimoto, *ACS Appl. Energy Mater.*, 2022, **5**, 4108–4116.
- [35] J. M. Chen, Y. Y. Chin, M. Valldor, Z. Hu, J. M. Lee, S. C. Haw, N. Hiraoka, H. Ishii, C. W. Pao, K. D. Tsuei, J. F. Lee, H. J. Lin, L. Y. Jang, A. Tanaka, C. T. Chen and L. H. Tjeng, *J. Am. Chem. Soc.*, 2014, **136**, 1514–1519.
- [36] T. Burnus, Z. Hu, H. Wu, J. C. Cezar, S. Niitaka, H. Takagi, C. F. Chang, N. B. Brookes, H. J. Lin, L. Y. Jang, A. Tanaka, K. S. Liang, C. T. Chen and L. H. Tjeng, *Phys. Rev. B.*, 2008, **77**, 205111.
- [37] N. Hollmann, Z. Hu, M. Valldor, A. Maignan, A. Tanaka, H. H. Hsieh, H. J. Lin, C. T. Chen and L. H. Tjeng, *Phys. Rev. B.*, 2009, **80**, 085111.

- [38] L. Han, X.-Y. Yu and X. W. (David) Lou, *Adv. Mater.*, 2016, **28**, 4601–4605.
- [39] H.-H. Zou, C.-Z. Yuan, H.-Y. Zou, T.-Y. Cheang, S.-J. Zhao, U. Y. Qazi, S.-L. Zhong, L. Wang and A.-W. Xu, *Catal. Sci. Technol.*, 2017, **7**, 1549–1555.
- [40] X. Xu, H. Liang, F. Ming, Z. Qi, Y. Xie and Z. Wang, *ACS Catal.*, 2017, **7**, 6394–6399.
- [41] B. Chen, Z. Yang, Q. Niu, H. Chang, G. Ma, Y. Zhu and Y. Xia, *Electrochem. commun.*, 2018, **93**, 191–196.
- [42] Y. Feng, X.-Y. Yu and U. Paik, *Sci. Rep.* 2016, **6**, 34004.
- [43] X.-Y. Yu, Y. Feng, B. Guan, X. W. (David) Lou and U. Paik, *Energy Environ. Sci.*, 2016, **9**, 1246–1250.
- [44] J. Nai, Y. Lu and X.-Y. Yu, *J. Mater. Chem. A*, 2018, **6**, 21891–21895.
- [45] N. Cheng, Q. Liu, J. Tian, X. Sun, Y. He, S. Zhai and A. M. Asiri, *Int. J. Hydrogen Energy*, 2015, **40**, 9866–9871.
- [46] S. Battiato, M. Urso, S. Cosentino, A. L. Pellegrino, S. Mirabella and A. Terrasi, *Nanomater.*, 2021, **11**, 3010.
- [47] G.-Q. Han, Y.-R. Liu, W.-H. Hu, B. Dong, X. Li, X. Shang, Y.-M. Chai, Y.-Q. Liu and C.-G. Liu, *Appl. Surf. Sci.*, 2015, **359**, 172–176.
- [48] C. Xia, Q. Jiang, C. Zhao, M. N. Hedhili and H. N. Alshareef, *Adv. Mater.*, 2016, **28**, 77–85.
- [49] G. Yilmaz, C. F. Tan, Y.-F. Lim and G. W. Ho, *Adv. Energy Mater.*, 2019, **9**, 1802983.
- [50] X. Li, G.-Q. Han, Y.-R. Liu, B. Dong, W.-H. Hu, X. Shang, Y.-M. Chai and C.-G. Liu, *ACS Appl. Mater. Interfaces*, 2016, **8**, 20057–20066.
- [51] Z. Zand, P. Salimi, M. R. Mohammadi, R. Bagheri, P. Chernev, Z. Song, H. Dau, M. Görlin and M. M. Najafpour, *ACS Sustainable Chem. Eng.*, 2019, **7**, 17252–17262.
- [52] K. Fan, H. Chen, Y. Ji, H. Huang, P. M. Claesson, Q. Daniel, B. Philippe, H. Rensmo, F. Li, Y. Luo and L. Sun, *Nat. Commun.*, 2016, **7**, 11981.
- [53] D. Wang, Q. Li, C. Han, Q. Lu, Z. Xing and X. Yang, *Nat. Commun.*, 2019, **10**, 3899.
- [54] P. Li, X. Duan, Y. Kuang, Y. Li, G. Zhang, W. Liu and X. Sun, *Adv. Energy Mater.*, 2018, **8**, 1703341.
- [55] K. Bera, A. Karmakar, S. Kumaravel, S. S. Sankar, R. Madhu, H. N. Dhandapani, S. Nagappan and S. Kundu, *Inorg. Chem.*, 2022, **61**, 4502–4512
- [56] H. S. Chavan, C. H. Lee, A. I. Inamdar, J. Han, S. Park, S. Cho, N. K. Shreshta, S. U. Lee, B. Hou, H. Im and H. Kim, *ACS Catal.*, 2022, **12**, 3821–3831.
- [57] B. Singh and A. Indra, *Dalt. Trans.*, 2021, **50**, 2359–2363.
- [58] J. Jiang, F. Sun, S. Zhou, W. Hu, H. Zhang, J. Dong, Z. Jiang, J. Zhao, J. Li, W. Yan and M. Wang, *Nat. Commun.*, 2018, **9**, 1–12.